Department of Physics
Faculty of Science

Multiply Stacked Graphene Heterostructures

Chong Yau Loong (A0074532J)

Supervisor: Prof. Barbaros Özyilmaz

Acknowledgement

The route to writing this final year project was not an easy task and I would like to take this opportunity to thank the following people, to whom I owe my sincerest gratitude.

First of all, I would like to thank my supervisor, Professor Barbaros Özyilmaz, for providing me with the opportunity to take part in this exciting project, and for his valuable feedback and patience throughout the entire project.

I would also like to express my gratitude to Eoin O'Farrell for generously sharing his expertise on the subject and for patiently guiding me on the various problems I encountered in the project.

At the same time, I would like to extend my gratitude to Tan Jun You, a talented, passionate senior, for his helpful feedbacks and supports at all of the time.

Last but not least, my thanks and appreciations also go to my family and friends for their continuous supports and helps throughout my university life.

Contents

Chapter 1 Introduction

1.1 Two-dimensional crystals

Dimensionality is one of the most defining material parameters. A material or compound can exhibit dramatically different properties depending on whether it is arranged in a 0D, 1D, 2D or 3D crystal structure.

Due to the limited thickness, the quantum confinement effect as well as the dominance of surface and interface states makes thin film exhibit special properties different from its 3D bulk counterpart. Unlike the 1D and 3D material, the researches on 2D material only become popular since the discovery of Graphene.

In nature, 2D crystals mainly exist as a form of layered materials with strong in-plane bonds and weak Van-der-Waals like coupling between layers. Based on this characteristic of layered materials, mechanical cleavage, such as the Scotch-tape cleaving technique can be used to isolate their atomic planes. Monolayer 2D crystals have only two surfaces but no bulk in between, which presents the extreme case of surface science. In other words, many of the theoretical existed 2D crystals are unlikely to survive in reality because they would corrode, decompose, segregate and so forth.

Although it remained unclear whether free-standing atomic layers could exist in principle, it has long been tempting for people to try splitting such layered materials into individual monolayer. Nowadays, there are more than a dozen of different 2D crystals being successfully isolated under the ambient conditions. Some of the famous examples are: graphene, hexagonal boron nitride (hBN), molybdenum disulphide (MoS_2).

1.2 Graphene Heterostructures

Research on graphene and other two-dimensional atomic crystals is intense and is likely to remain one of the leading topics in condensed matter physics and materials science for many years. Looking beyond this field, isolated atomic planes can also be reassembled into designer heterostructures made layer by layer in a precisely chosen sequence.

Heterostructures device are made by stacking different 2D crystals on top of each other. The resulting stack represents an artificial material assembled in a desire sequence. Within the whole structure, the strong covalent bonds provide in-plane stability of 2D crystals while the Van-der-Waals-like forces keep the stack together.
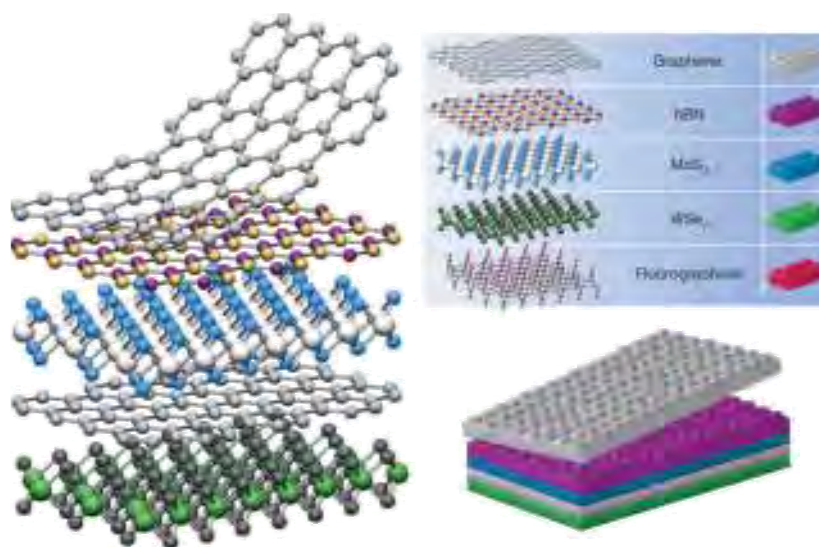
Figure 1.1 Building of Van der Waals heterostructures.

Although the principles behind heterostructures remain unclear and complicated, various experiments have shown that individual layers of very different characteristics can be combined via the proximity effect and the results are promising. There exist many 2D materials, which provide a large range of different interesting properties. Thus, the heterostructures are capable to offer even greater scope for future research and fit an enormous range of possible applications.

1.3 Graphene versus MoS$_2$

Among all the candidates in the current 2D library, graphene exhibit the highest mechanical strength and electronic quality. However, graphene by itself might not be so useful, for example: it is lack of band gap, poor spin orbit coupling etc. Thus heterostructure is one of the solutions to compensate for graphene's weaknesses or enhance the existing properties. By placing graphene on top of other crystalline, a unique graphene heterostructure is created, in which the electron in graphene may ends up exhibit some interesting new properties.

In contrast to graphene, molybdenum disulphide is a semiconductor with a relatively large band gap and demonstrated slightly lower mobility comparing to graphene. Interestingly, its inversion symmetry breaking and high spin orbit coupling in molybdenum disulphide produces a giant valley dependent spin splitting with quantization axis along the out-of-plane direction. While increased spin orbit coupling usually results in shorter spin lifetime, which is indeed undesirable in application.

1.3.1 Graphene

Graphene is a 2 dimensional crystalline allotrope of carbon, in which the carbon atoms are densely packed in a regular sp2-bonded atomic scale hexagonal pattern. Graphene can be described as a one-atom thick layer of graphite and it is the basic structural element of other carbon allotropes, such as fullerenes (1D), carbon nanotubes (2D) and graphite (3D).

High quality graphene is mechanically strong, light, nearly transparent, excellent conductivity of heat and electricity and long spin diffusion length. However, graphene is lack of band gap and having poor spin orbit coupling.
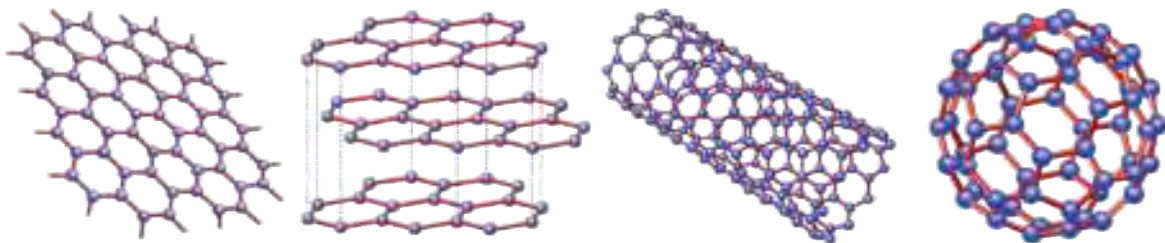

Figure 1.2: Graphene, Graphite, Carbon nanotube, Fullerene

Carbon has four valence electrons occupying the 2s and 2p orbitals in the elemental form. In graphene, carbon atoms undergo the sp^2 hybridization, in which a 2s orbital is mixed with

only two of the three available 2p orbitals. As a result, a total of three sp^2 orbitals are formed in the *xy*-plane and leaving a 2p$_z$ orbital. Each carbon atom in the graphene lattice is connected to its three nearest neighbours by strong in-plane covalent bonds. These are known as the σ bonds and which is formed by the three sp^2 electrons. The fourth 2p$_z$ orbital, which h is perpendicular to the plane of the graphene sheet, thus it does not interact with the in-plane σ electrons. The 2p$_z$ orbitals from neighbouring atoms overlap resulting in delocalized π (occupied or valence) and π* (unoccupied or conduction) bands, which contribute to most of the electronic properties of graphene.

The band structure of monolayer graphene can be adequately described using a simple nearest neighbour tight-binding approach considering a single π electron per atom. The resultant dispersion relation can be written as:

$$E^{\pm}(k_x, k_y) = \pm\gamma_0 \sqrt{1 + 4\cos\frac{\sqrt{3}k_x a}{2}\cos\frac{k_y a}{2} + 4\cos^2\frac{k_y a}{2}}$$

hence, the band structure of graphene is visualized and shown in Figure 1.3.
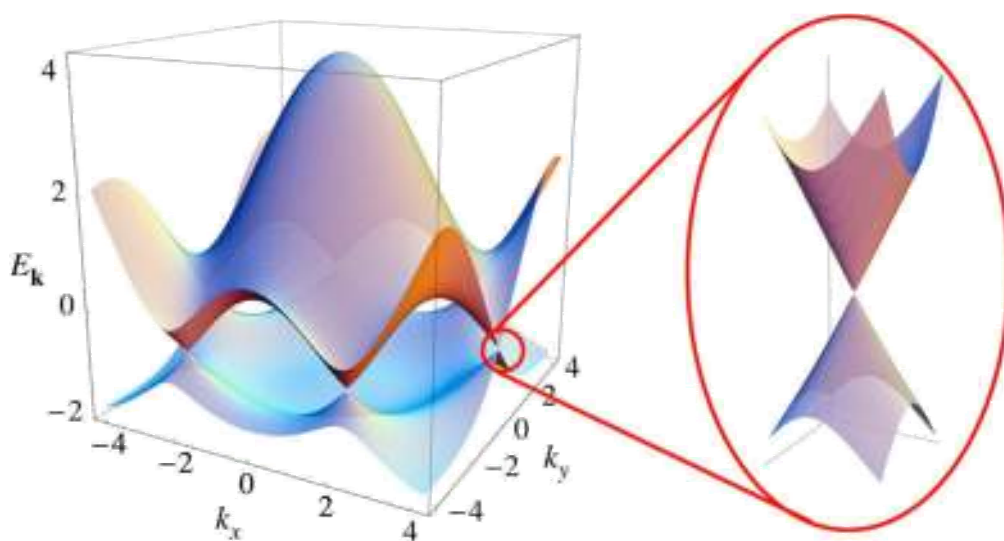

Figure 1.3: Band structure of graphene showing the conductance and valence bands meeting at the Dirac point. Inset: One of the Dirac cone showing the linear dispersion relation at small values of *k*.

In intrinsic, un-doped graphene, each carbon atom contributes one electron completely filling the valence band and leaving the conduction band empty. In such case, the Fermi level (E_F) is

located exactly at the energy where the conduction and valence bands meet. These are known as the Dirac or charge neutrality points.

The occupied valence and empty conduction bands meets at Dirac point at which the density of states (DOS) is zero. Therefore, graphene is considered as a zero-gap semiconductor, with vanishing DOS at the Dirac point but no energy gap between the valence and conduction bands.

1.3.2 Molybdenum Disulphide

Before it is studied extensively, molybdenum disulphide is a well-known solid lubricant widely used in industry. Similar to graphite, MoS_2 has this lubricating ability because it is also composed of sheets of atoms stacked upon one another, with each sheet loosely bound to the next. The basic unit of MoS_2 is composed of a molybdenum atom coordinated with six sulphur atoms It is organized in two layers of sulphur atoms forming a sandwich structure, with a layer of molybdenum atoms in the middle. Each sulphur atom is coordinated with three molybdenum atoms within a single 2D layer of MoS_2. The bulk material is formed of these 2D layers held together by van der Waals forces.
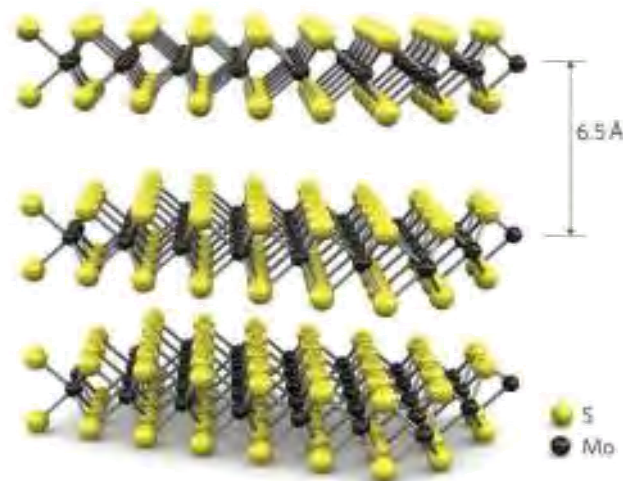

Figure 1.4: Atomic structure of layered hexagonal MoS2

Molybdenum disulphide belongs to the family of Transition Metal Dichalcogenides (TMDs), a semiconductor with strong spin-orbit interactions, and coupled spin-valley degrees of freedom. Electron-electron interaction effects are important in TMD semiconductors because of their in-plane effective masses are comparatively large (m^*~0.4). In practice, TMDs have been mostly used as channel material in field effect transistors (FET), in both top and back

gated configurations, showing intrinsic mobility at room temperature up to 50 $cm^2/(V \cdot s)$ and more than 10^5 on/off ratio.
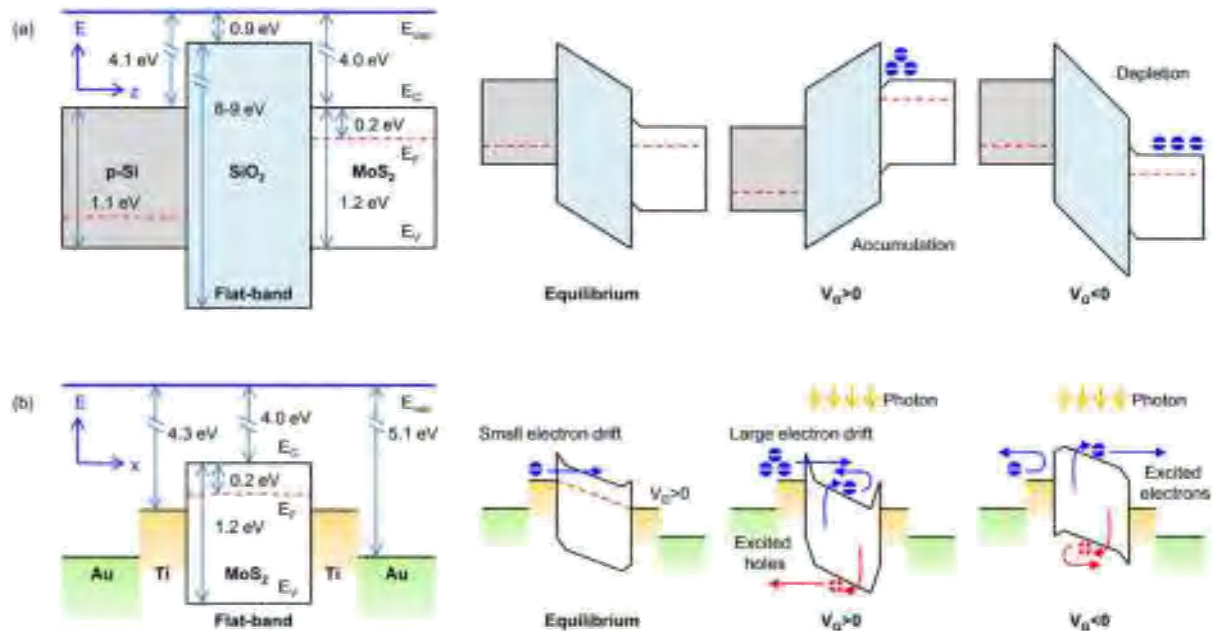

Figure 1.5: The use of MoS$_2$ in (a) FET and (b) Light sensor. The electronics properties can be realized as a common semiconductor with a band gap.

Besides, TMDs are attractive for optoelectronic application because of their high photoresponsivity. This property is characterized by a thickness modulated band-gap, which are indeed attractive for optoelectronic applications. From Figure 1.6, bulk MoS$_2$ is characterized by an indirect band gap and the direct excitonic transitions occur at higher energies at K point. By reducing the layer thickness, the indirect band gap becomes larger, while the direct excitonic transition barely changes. For monolayer MoS$_2$, it becomes a direct band gap semiconductor, thus it possess a stronger photoluminescence effect.
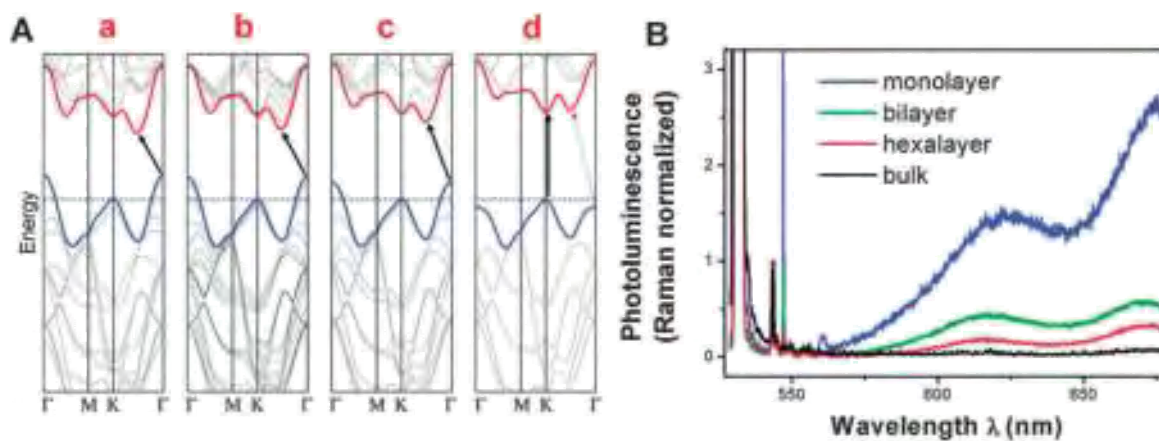
Figure 1.6: (A) Calculated band structures of (a) bulk, (b) quadric-layer, (c) bi-layer, and (d) monolayer MoS$_2$. The arrows indicate the lowest energy transitions. (B) Photoluminescence spectra normalized by Raman intensity for MoS2 layers with different thickness.

Figure 1.7: Photoluminescence effect. Red dotted lines indicate the monolayer MoS$_2$. Photos are taken by Nikon Eclipse LV100DA, epi-Fluorescent Microscopy 2 with external mercury lamp source and 10s exposure.

Nonetheless, the intrinsic electronic properties of MoS2, and particularly the role of electron-electron interaction in these materials remain largely unexplored.

Interestingly, both graphene and molybdenum disulphide are having properties which are compliment to each other (Table 1.1). Thus, it is a good idea to create a heterostructures out of these two materials, and this the beginning of the motivation of this project.

Graphene	MoS$_2$
No band gap	Band gap ~ 1.8eV
High mobility	Low mobility
No/Low spin-orbit-coupling	Strong spin-orbit-coupling
Long spin diffusion length	Short spin diffusion length

Table 1.1: Summary of the properties of graphene and MoS$_2$.

1.4 Motivation

Combining the electronic properties of graphene and molybdenum disulphide in hybrid heterostructures offers the possibility to create devices with various functionalities. Graphene-MoS$_2$ heterostructures are having great potential in the application of spintronics, flexible electronics, photo-electronics, as well as other interesting effects. Therefore, a graphene-MoS$_2$ heterostructures with an atomically clean interface is essential in providing a pathway toward the fabrication new devices and research.

This project is devoted to fabricate and characterize graphene-MoS$_2$ heterostructures. In this project, graphene will be transferred onto a few-layers MoS$_2$ to form the heterostructures by using the dry transfer techniques. Subsequently, several tools such as the AFM, Raman spectroscopy and also the electrical measurements will be used to characterize the heterostructures created.

Chapter 2 Characterization Techniques

2.1 Optical Microscopy

Optical microscope is a well-established technique which in the first place can be used for surveying large area graphene samples due to the technique's simplicity. In fact optical microscopy allows for a quick thickness inspection before using more precise tools such as Raman spectroscopy, atomic for microscopy (AFM) etc.

All of our graphene and MoS_2 samples are prepared via the mechanical exfoliation, and optical microscope provides a fastest for us to search and locate suitable flakes on a piece of wafer. In this section, we will use graphene and MoS_2 as the research objects to illustrate the characteristic of optical microscopy.

2.1.1 Graphene

Graphene is a single layer of carbon atom array, and it is said to be invisible in some cases. Graphene visibility using optical microscopy is usually explained by the change of the interference colour of reflected light from graphene with respect to the empty substrate as well as by graphite's opacity. Therefore, by manipulating the substrate (such as material used or thickness) that supports graphene, it is possible to enhance graphene's visibility under the optical microscope.

The most popular substrate surface on which graphene becomes visible is a silicon wafer with layer of silicon dioxide. It has been shown that 90nm and 300nm of SiO_2 layer give graphene a highest contrast under white light.

However, working directly on SiO_2 surface is not favoured for the dry transfer process, which will be discussed in the next chapter. Instead of bare SiO_2 surface, graphene will be deposited on a Si wafer spin-coated with a few layers of polymers. These polymers act as the releasing layer and supporting layer which they are required for the dry transfer process. Due to the introduction of these additional layers of polymers, graphene is almost invisible in such system, thus making the task of sample preparation become more difficult and time

consuming. Fortunately, with the help of colour filter, the contrast of graphene is slightly improved, but it is not very effective.
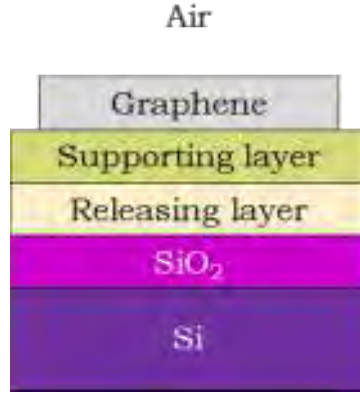

Figure 2.1 Optical systems with n=6 layers

To overcome this difficulty, the thicknesses of the polymers are adjusted so that the contrast of graphene is optimized. To do so, we reproduced the calculation done by Blake et al. at 2007, and generalized the system up to *n*-layers. In our model (Figure 2.1), we assume the use of reflected light microscope, with both the incident light and reflected light perpendicular to the sample.

By Fresnel's equations, interface between k and (k+1) layers is described by relative amplitude of reflected wave, which is given by:

$$r_k = \frac{n_{k+1} - n_k}{n_{k+1} + n_k}$$

Where n_k represent the refractive index of kth layer's material. Optical path covered by light in *k*-layer is defined as:

$$\Delta_k = \frac{4\pi}{\lambda} n_k d_k$$

Where d_k is the thickness of kth layer. Relative amplitude of reflected light from the system with k interfaces is then:

$$re_{(k)}^{i\varepsilon} = \frac{r_{k-1} + re_{(k-1)}^{i\varepsilon} e^{-i\Delta_{k-1}}}{1 + r_{k-1} re_{(k-1)}^{i\varepsilon} e^{-i\Delta_{k-1}}}$$

Where $e^{i\varepsilon}$ represent the phase.

Thus, the reflectance of system with k interfaces is given by:

$$R_{(k)}(\lambda) \equiv \frac{I_{(k)}(\lambda)}{I_0(\lambda)} = \left| re_{(k)}^{i\varepsilon} \right|^2$$

Where $I_0(\lambda)$ is the intensity of incident light. Suppose the jth represent graphene (or any other material we are interested to characterize), optical contrast of graphene for the system is:

$$C(\lambda) = \frac{I(\lambda)|_{without graphene} - I(\lambda)}{I(\lambda)|_{without graphene}} = \frac{I_{(k)}(\lambda)\big|_{n_j=1, d_j=0} - I_{(k)}(\lambda)\big|_{n_j=2.6-1.3i, d_j=0.37nm}}{I_{(k)}(\lambda)\big|_{n_j=1, d_j=0}}$$

It is obvious that the contrast is dependent on the wavelength of incident light.

Back to our model as describe in Figure 2.1, the thicknesses of both supporting layer and releasing layer is characterized by the rotational speed during spin-coating process which can easy be manipulate. Other relevant parameters such as the viscosity, refractive indexes are obtained from manufacture data sheet. In practice, we used PMMA as the supporting layer, and varying the thickness of PMMA for maximum graphene visibility under certain colour of light. The result is shown in Figure 2.2.

Normally, a particular thickness of PMMA is chosen so that the contrast is optimized for green or yellow light. That is because human eye is more adapted to these colours. Figure 2.3 shows the actual comparisons between the contrasts of graphene at different colour of incident light. This model works well for magnification from 5X to 20X, while a slight discrepancy is observed for 50X and 100X. This is because in our model, the optical path in the microscope is not considered. Both 50X and 100X use more powerful and thicker lens, thus, their refractive contributions to the light path become significant comparing to 5X, 10X and 20X that use a smaller lens. Nevertheless, this issue is less bothering as searching of graphene is usually done at 5X magnification.
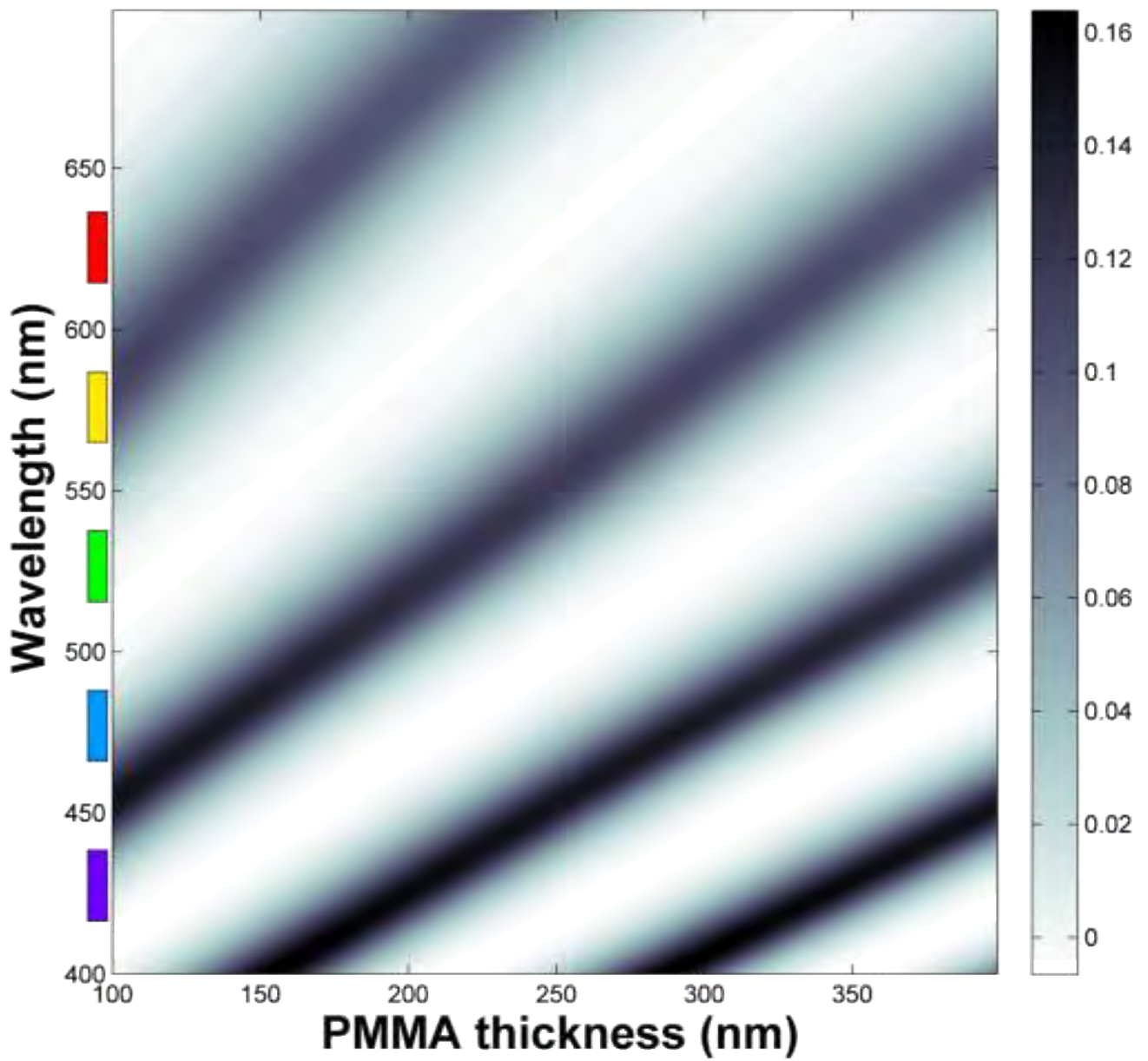
Figure 2.2: The plot showing the contrast of graphene at each wavelength and PMMA thickness. The colour scale bar at right represents the contrast.
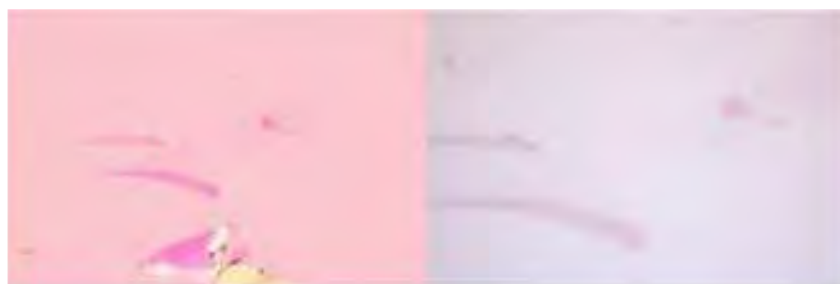
Figure 2.3: Graphene observed at (left) 20X and (right) 100X. PMMA thickness is ~270nm
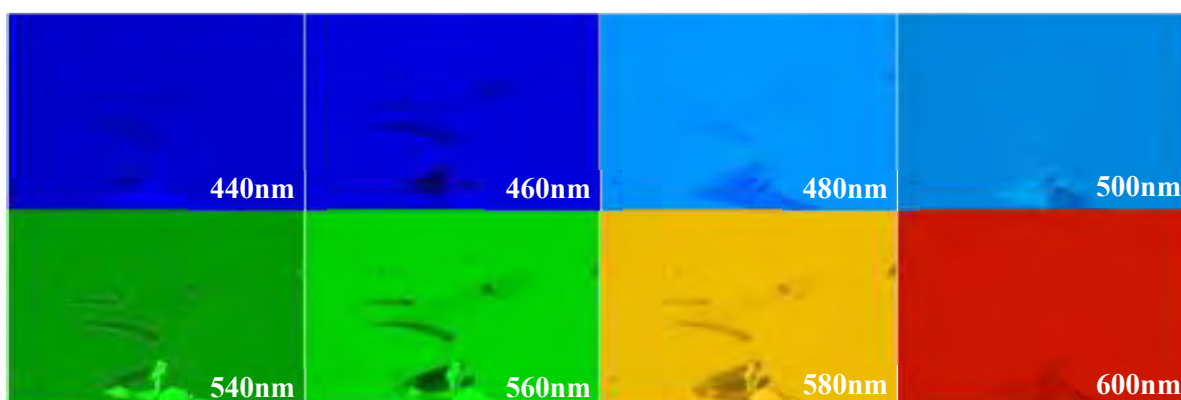

Figure 2.4: Contrast of graphene under different colour light at 20X magnification. Best contrast is observed at 560nm.
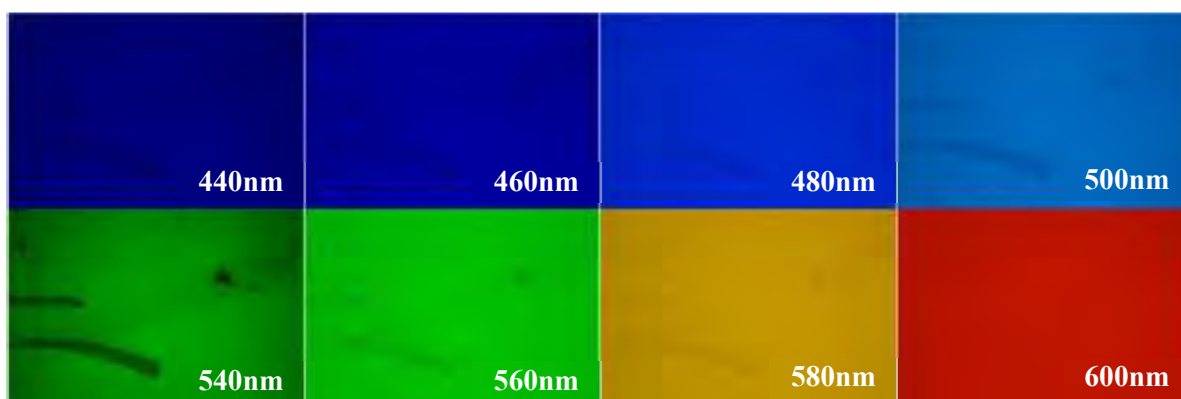

Figure 2.5: Contrast of graphene under different colour light at 100X magnification. Best contrast is observed at 540nm, which is slightly lower than at the case of 20X.

With this generalized program, characterization process can be made easy almost for any crystals or any substrates.

2.1.2 Molybdenum Disulphide

In this project, the MoS_2 is used as the substrate for graphene in the heterostructures. Due to the difficulty of obtaining monolayer MoS_2 crystal via the mechanical exfoliation, the thickness of the flake used are usually around 5-10nm. Throughout this section, we will illustrate the criterions in the selection of suitable MoS_2 flake via optical microscopy.

i) Size

Unlike graphene, it is not easy to obtain a good MoS_2 flake that is suitable for making the heterostructures. At most of the time (~80%), the size of the thin MoS_2 flakes are way too small (<10μm), which is not favoured as it will make device fabrication process (such as electron beam lithography) become more challenging. This criterion in fact does apply to graphene as well, but since we can always obtain graphene with large area, thus it does not concern us very much in that case.

Generally, the size of the MoS_2 must be at least 2x4μm as it is the minimum required size for us to fabricate a basic 6-probes device. However, in practice, due to the uncertainty of the bubbles distribution after graphene is transferred onto it via the dry transfer technique (Chapter 3), we require the area to be as large as possible. Typically, we will select the flakes with area larger than 10x10μm.

ii) Thickness

Few-layers MoS_2 flakes are blue in colour on SiO_2 substrate, and it can be observed easily under microscope without any help from colour filters. Interestingly, the colour of the flakes is depending on its thickness. Based on this characteristic, the table below summarize the variation of MoS_2 flake's thickness and their respective colour. The table was constructed by extracting the photo of MoS_2 samples taken at same brightness and exposure time while the thickness is determined by AFM. More samples are inspected to verify the consistency of the table, which are indeed able provide a fast and efficient estimation of the thickness.

Normally, there are some limiting factors on the thickness that we need to consider when we looking for the suitable MoS_2 flake. First, when gold is deposited across the MoS_2 to create

electrical contacts, a thicker flake will increase the chance of getting bad connections. Second, some interesting properties of MoS_2 may be weakened as number of layers increases. One example would be the bands splitting in thin MoS_2 allow us to achieve spin dependent transport, and the splitting starts to change after 10 layers. Therefore, we will disregard the flake with thickness larger than 10nm (~15 layers).
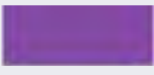
	Colors	Thickness (nm)	# layers
a		1.7	3
b		5.0	7
c		5.5	8
d		6.0	9
e		6.7	10
f		7.5	11
g		8.2	12
h		9.0	13
i		9.6	14

Table 2.1: The colour variation of few-layers MoS_2 crystals with different thickness on 300nm SiO_2 substrate.
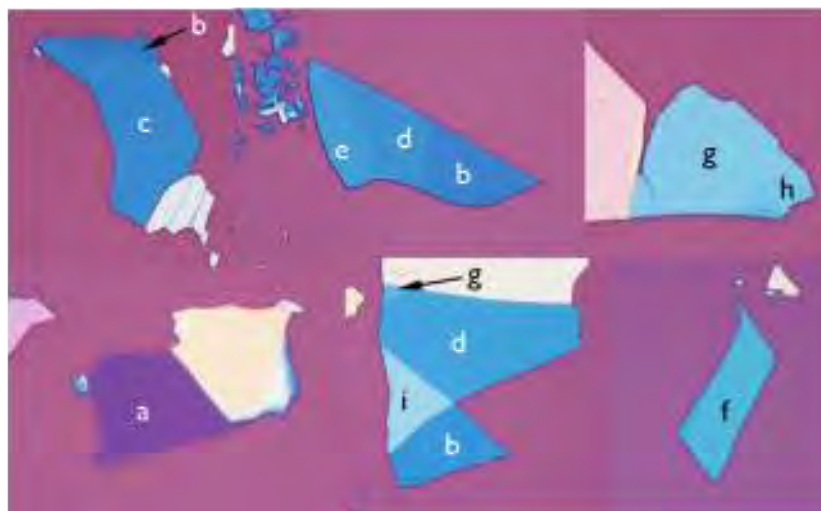
Figure 2.6: MoS_2 crystals with different thicknesses.

iii) Surface cleanliness

The surface of any freshly prepared samples might contain certain amount of contaminants, such as dust, hydrocarbons, or glue residues (especially for sample prepared via Scotch tape method). Usually, direct observation of these contaminants is not obvious especially when they are too small, transparent or having similar colour to the substrate. Therefore, microscope equipped with dark field illumination provides a more effective observation of such surface adsorbates.

The dark field microscopy works by illuminating the sample with light that will not be collected by the objective lens, and thus will not form part of the image. This produces the classic appearance of a dark, almost black, background with bright objects on it.
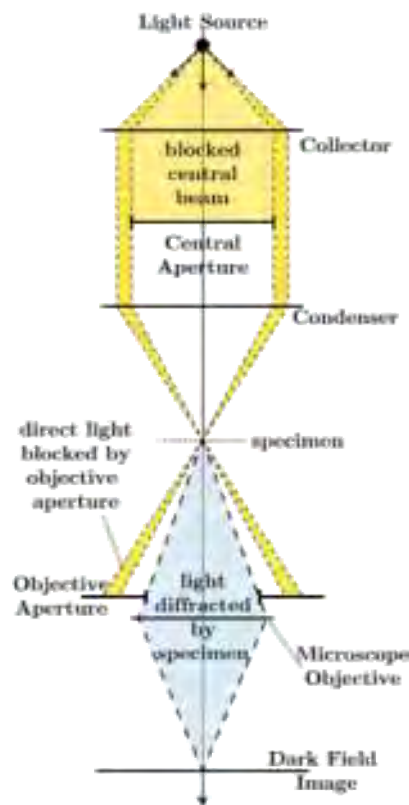
Figure 2.7: Schematic diagram of the light path through a dark field microscope. In this case, a transmission light microscope.

From Figure 2.7, the scattered light enters the objective lens, while the directly transmitted light simply misses the lens and is not collected due to a direct illumination block near the light source. In the end, only the scattered light goes on to produce the image, while the directly transmitted light is omitted. As height differences in the samples will scatter the

incident light, therefore only the edges of the samples will be illuminated, and the brightness is proportional to the thickness. Figure 2.8 shows a typical image of dark field microscopy of thin MoS_2 flake, having a small contaminant which is not observed in bright field image.

Figure 2.8: Typical dark field microscopy image (right).

Throughout this section, we have seen optical microscopy as a versatile tool for characterization. It provides an effective way to survey a large area (2X2 cm) in a very short time. However, its resolution is limited, thus once we have located a suitable flake at a smaller area (30X30μm), and AFM will then be used to explore the detailed height profile of the sample.

2.2 Atomic Force Microscopy

Atomic force microscopy allows 3D profiling of surfaces at the nanoscale. The working principle of AFM is accomplished by measuring the forces between a sharp tip, usually less than 10nm, and close to the sample surface at distance ~0.2-10nm. The probe is fabricated on a cantilever, usually made of silicon nitride. By reflecting a laser beam off the cantilever into a sensitive photodiode array, the cantilever deflections that occur as the tip movers over the sample can be determined. The deflections (the height, z) is recorded as the function of the sample's X and Y positions, thus a three dimensional image of the sample's surface can be modelled.
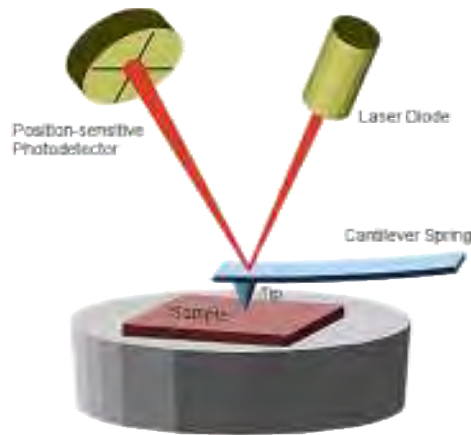
Figure 2.9: Basic components of a typical AFM.

There are two primary imaging modes are normally used:

i) Contact mode AFM:

In this mode, the tip-sample distance (typically less than 0.5nm) leads to a repulsive Van der Waals forces. By keeping a constant cantilever deflection, which is achieved by the feedback loops, the force between the tip ad the sample stays at constant and allows an image of the surface to be obtained. Unfortunately, as the tip is very near to the sample when operating, sometimes it will damage the sample surface.

ii) Tapping mode AFM:

This mode is similar to contact mode, with the differences are that the cantilever oscillates at its resonant frequency and the tip-sample distance varies between 0.5-2nm. A small piezoelectric element mounted on the tip holder drives the oscillation. An image is obtained by maintaining a constant oscillation amplitude, which provides a constant tip-sample interaction. Unlike contact mode, this mode is good for high resolution imaging of sensitive sample as it is less likely for the tip to damage the surface due to the larger tip-sample distance.

In this project, AFM is used as an imaging tool to inspect the surface topology and the height profile of both the graphene and MoS_2 samples. As an effort to minimize the interface contaminants trapped within the interface of heterostructures, a more detailed scan will be carry out on the selected MoS_2 flakes to ensure the surface cleanliness.
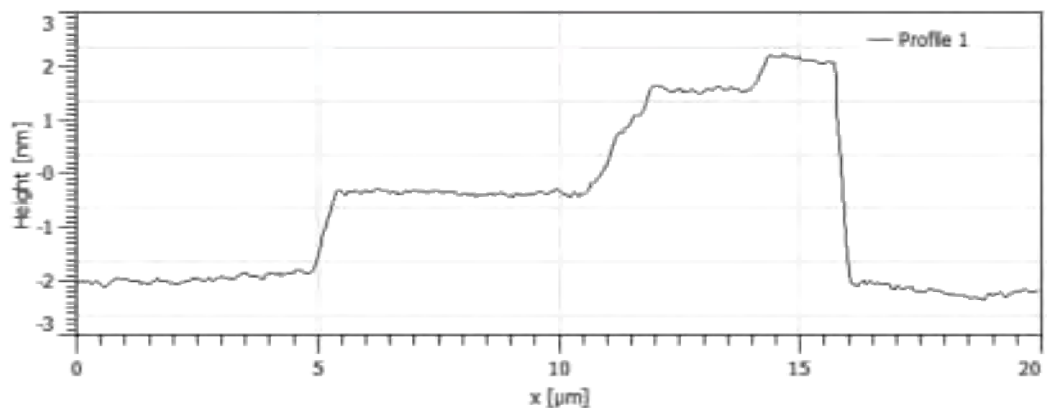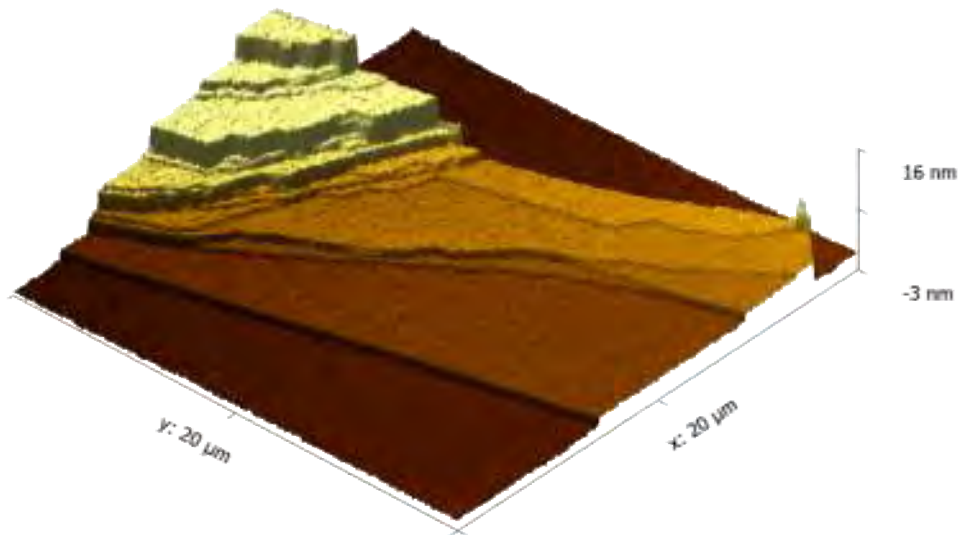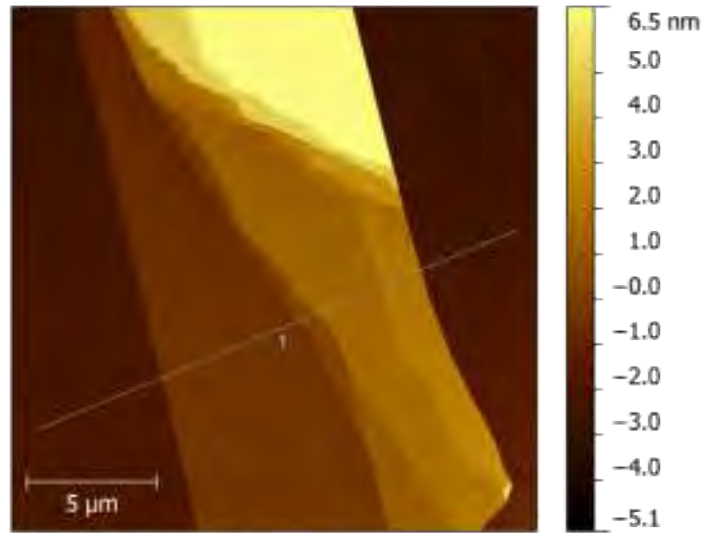
Figure 2.9: AFM topography imaging of a MoS$_2$ flake.

2.3 Raman Spectroscopy

Raman spectroscopy is a spectroscopic technique where the inelastic scattering of monochromatic light, typically from a laser source interacts with a sample. During Raman measurements the sample is irradiated with a laser source, the scattered light is then gathered and sent through a spectrophotometer to obtain a Raman spectrum.

In this process the sample absorbs the incoming photons and then re-emits them with the same or different frequency. Most of the scattered light has the same frequency as the incident light and hence, there is a very strong elastic scattering named Rayleigh scattering. The second scattering process is inelastic, and has an altered and shifted frequency which is known as the Raman scattering. The characteristic of Raman shifts provide valuable information about vibrational, rotational and other low frequency changes in the samples.

2.3.1 Graphene

In the case of graphene, the Raman signal variations observed for different numbers of graphene layers not only demonstrate changes in the electron bands but also provide an easy and non-destructive means to distinguish single and few-layer graphene.

The most prominent Raman features from graphene are the so-called G mode and 2D mode as shown in Figure 2.10. The G mode resides around $1580cm^{-1}$ and the 2D peak sits around $2700cm^{-1}$. Two further peaks can also be observed; the D peak may appear at $\sim1350cm^{-1}$ and G* peak at $\sim2450cm^{-1}$. In terms of their vibrational character, the G mode corresponds to bond strectching of all pairs of sp^2 atoms in both rings and chains, whereas the D mode arises due to the breathing modes of sp^2 atoms in rings. Usually the D mode is a forbidden transistion, however in the presence of disorder symmetry is broken (defects) and the transistion is allowed. Therefore, we can make used of this characteristic to detech any defects in our graphene samples before and after transfer.
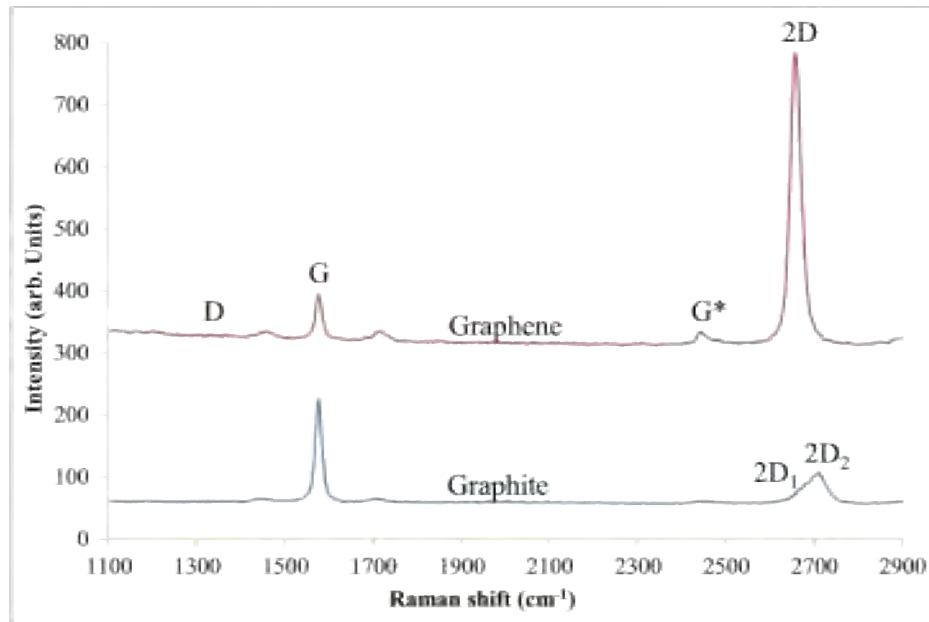
Figure 2.10: Raman spectrum of graphene and graphite (>5 layers graphene), obtained using a 531nm green laser.

2.2.2 Molybdenum Disulphide

Similar to graphene, single-layer molybdenum disulphide has distinctive signatures in its Raman spectrum comparing to the Raman spectrum of bulk MoS_2. The Raman spectrum of bulk MoS_2 has two prominent peaks: an in-plane (E_{2g}) mode located around $387cm^{-1}$ and an out-of-plane (A_{1g}) mode which is located at $415cm^{-1}$. The in-plane mode corresponds to the sulphur atoms vibrating in one direction and the Molybdenum atom in the other, while the out-of-plane mode is a mode of just the sulphur atoms vibrating out-of-plane.

As MoS_2 becomes thinner, these two modes evolve with thickness. The in-plane mode upshifts to $391cm^{-1}$ and the out-of-plane downshifts to $411cm^{-1}$. Therefore, the difference of these two modes can be used to identify the thickness of the MoS_2 flakes, especially for monolayer MoS_2 ($\Delta \approx 20cm^{-1}$).

Figure 2.11: Raman spectra of exfoliated MoS_2 flakes on SiO_2/Si substrate with thickness reducing from 25nm to 1.3nm. As the thickness decreases, the shift between E_{2g} and A_{1g} become shorter. The intensities are scaled to fit them in ascending order according to their thickness (i.e. higher intensity→thicker MoS_2)

Chapter 3 Transfer Techniques

3.1 Transfer Procedures

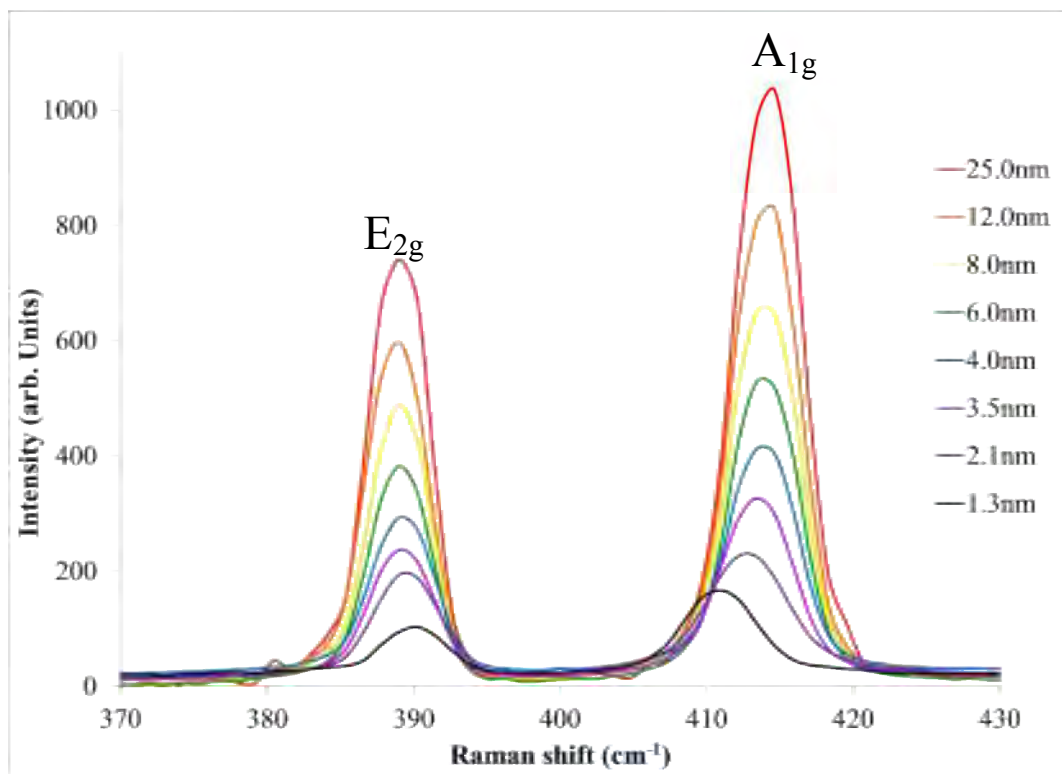Before we begin with the device fabrication, we need to build the graphene-MoS_2 heterostructures and also get it characterized. Thus, the major part in this project is to stack graphene on top of molybdenum disulphide flake, and to ensure the level of interface contaminations is reduce to minimum. Also, thanks to the flexible properties of graphene, this effectively minimized the mechanical damage due to the transfer process and the quality of graphene can be maintained.

In this project, both graphene and MoS_2 are prepared via the mechanical exfoliation which their size are very often limited to 10-20μm. Due to the small size of both materials, exfoliation of graphene directly on top of MoS_2 is impractical. Therefore, in order to create such heterostructures, it is necessary to perform a precise transfer process to stack and align graphene flakes from one substrate to the different target substrate (MoS_2)

Currently, there are many transfer techniques developed by so many research groups around the world, but most of them can be classified into two types, that are: the wet transfer and dry transfer. For the wet transfer, as its name suggest, it required a wet intermediate step during the transfer process. In this case, the flake to-be-transferred will need be to in contact with liquid such as water or other solution before it is transferred onto another substrate. Therefore, the chances for contaminants being trapped within the interface of the flake and target substrate are very high and difficult to remove, and hence deteriorate the quality of the devices. However, comparing to the dry transfer technique, the wet transfer is relatively easy to perform, thus this method is still widely used by many people.

 In this chapter, we will discuss the ideas of the transfer techniques and the major steps involved and finally the transfer results. Throughout the project, we will only prepare our heterostructures via the dry transfer technique, developed senior in our group. A brief discussion of the wet transfer will be introduced as a background context. Finally we will make comparisons with the dry transfer method and explain why this method is chosen and how can it improve and enhance the device's quality.

3.1.1 General Frameworks of Transfer Procedures

Very often, almost all of the transfer techniques involved several steps which are similar to each other, but with some modifications to suit ones research interest. In this section, we will give a brief overview of a general steps for transfer procedure.

i) Preparation works

First of all, we need to prepare the sample of the 2D crystals which we want to stack to form the heterostructures. They can be prepared by mechanical exfoliation from its bulk crystals, or growth by chemical vapour deposition (CVD). Depends on the transfer types, the sample may have to be prepared on some other polymer substrate instead of Si wafer.

ii) Introduce of supporting film layer

This is crucial part of the transfer process. Because of the flake involved are usually very small, this supporting layer act as a medium for us to 'peel' the graphene off from its original substrate and stack it onto another crystal in an easier way. The film material must be flexible or strong enough so that it can hold the graphene firmly and not cracked during the process. Usually, the material used for the supporting layers are chosen to be transparent to ease the processes in the next step. One example of material with such properties is of Poly-methyl methacrylate (PMMA), which is a transparent thermoplastic and can be dissolved by acetone. The polymer is deposited via the spin-coating method, and its mechanical properties vary with its thickness, which can be easily controlled by the rotation speed as well as the temperature of hard bake and the baking duration.

iii) Alignment

Before we start the alignment, the supporting layer must be separated from the original substrate which might involve some lift off process. After an isolated film which holding the desire graphene is obtained, which is then attached to the arm of a manipulator, and place above the new substrate with the surface of the graphene facing the new substrate. The alignment is usually done with the aid of video microscope. As the film is transparent, we can adjust the focus of the microscope to either the graphene (on the suspended film) or the substrate crystal. By making use of the focus and the video output functions of video microscope we can first focus to the substrate crystal and its exact location is marked and recorded. Next, we change the focus to the graphene on suspended film, by keeping the

substrate in stationary, the manipulator is adjusted so that the position of graphene match the marked region we obtained earlier. Finally, the film and substrate is brought into contact by lowering the arm of manipulator and the film will adhere to the substrate's wafer.

iv) Removal of film material

Finally, the film is removed by using the appropriate chemical, leaving only the heterostructures. For example, acetone is used to remove PMMA.

3.1.2 Wet Transfer Method

As mentioned earlier, there are many versions of wet transfer techniques being developed and here we will introduce one of the methods that widely used in our lab with a little customization.

i) Preparation of flakes

The process begins with the mechanical exfoliation of substrate crystal (such as MoS_2, hBN) directly onto a Si wafers. With the help of optical microscope, a suitable substrate is found and located. Meanwhile, graphene is exfoliated onto another Si wafer with 300nm thermally growth SiO_2. A suitable size of graphene is located by the optical microscope and verified by using Raman spectroscopy.

ii) Spin coating of supporting polymer

The wafer containing graphene is then spin coated with a certain thickness of PMMA. After spin coating, a tape with a tiny windows cut away is adhere to the PMMA surface, where the window expose location of the desire graphene flake. The tape and PMMA film serves as a holder and supporting layer for graphene, so that we can separate graphene from the original Si wafer, and proceed to the next step of transfer.

iii) Lift off of film

Next, KOH solution is used to etch the SiO_2 layer between graphene and Si wafer, so that the PMMA film holding the desire graphene flake will be isolated from the wafer. Due to the hydrophobic properties of PMMA, the film will float on the solution surface while the wafer will sink to the bottom. After that, the film is rinsed by deionized water to remove most of the

KOH and dried by using a piece of cleanroom cloth. The film with the tape as holder is then carefully attached to the arm of micromanipulator.

iv) Alignment of flakes and the actual transfer

Now, the suspended PMMA film is placed above the substrate's wafer we prepared earlier. With the help of the video microscope, the position of the graphene flake on the PMMA film is precisely aligned with the position of the target substrate crystal flake. Next, the film is then brought into contact with the substrate's wafer. The target substrate's wafer is heated to temperature around 100C, so that PMMA film can adhere easily.

v) Removal of PMMA

Finally, the wafer is rinsed by acetone to remove the PMMA and the transferred sample is ready for characterization and device fabrication.

In this version of wet transfer, it can be seen that the graphene was in contact with KOH, therefore the higher chance for interface contaminations is inevitable. Therefore, in order to reduce the contaminations within the interface and produce better quality devices, the dry transfer method is highly favoured.

3.1.3 Dry transfer method

The dry transfer process is more or less similar to the wet transfer, but in this case the graphene will not in contact with any other liquid.

i) Preparation of flakes

First of all, the flakes are prepared by mechanical exfoliation as well. Similar to wet transfer, the substrate crystal is exfoliated onto the Si wafer and a suitable flake is located and characterized. Meanwhile, graphene is exfoliated onto another Si wafer which was previously spin-coated with different layers of polymers. The roles of the polymers in this technique are to serve as the supporting layer and the releasing layer. This procedure raised another challenge to us as the contrast of graphene is significantly decreased which make the searching process become harder (c.f. Chapter 2). Also, in compare to SiO_2 surface, graphene usually adhere poorly to most of the polymers, thus the yield and size of graphene are also

decreased badly. Normally, PMMA is used as the supporting layer and it can be dissolved by acetone, while the releasing layer, located at the middle of the system, which is chosen to be a different material, and it can only be dissolved by different solution other that acetone.
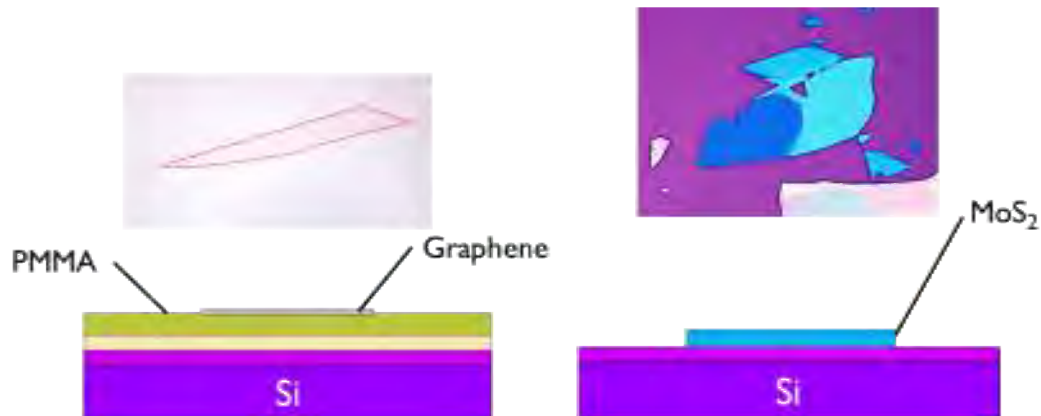

ii) Lift off process

Due to the introduction of releasing layer and exfoliation of graphene above the PMMA, the separation of PMMA film and the substrate can be done without making graphene in contact with any liquid solution. This is achieved by injecting developer solution from the edges, which then dissolve the releasing layer, thus the PMMA film holding the graphene on top is then separated from the system. Next, we use a holder (in our case, we used a tiny washer for convenient) support the suspended PMMA film from the bottom.
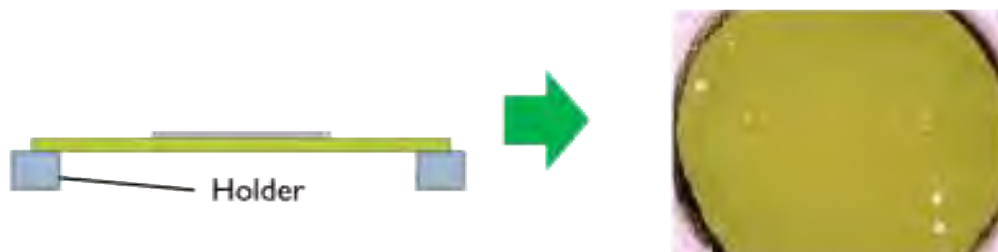
iii) Alignment and actual transfer

Similar to wet transfer techniques, the film which we have attached on the washer is inverted and placed on the arm of manipulator above the wafer which contains the substrate crystal we prepared in the earlier time. Again, the substrate wafer is heated, and the alignment is done by the help of video microscope. Once, the precise alignment between graphene and substrate crystal is done, the arm of manipulator is slowly brought down so that graphene is brought into contact with the target substrate crystal.
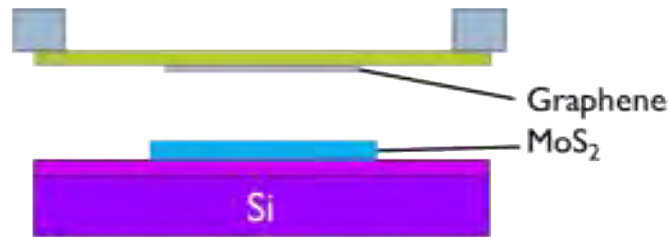
iv) Removal of PMMA

Finally, the PMMA is washed away by using acetone. Then, the heterostructures is ready for further characterizations and fabrications. Normally in this stage, we observe a higher chance that part of the transferred graphene will detach and scroll after PMMA layer is removed.

We can see that, throughout this process graphene was not contacted with any other liquid solution before it was brought into contact with the substrate crystal. Hence, the amount of contaminations at the interface is significantly reduced.

However, despite the benefit of the dry transfer, graphene is still has to be in contact with the cleanroom air, which might not be so perfectly clean. We will discuss more about some unavoidable limitations and some possible ways to improve the process in the later sections.

3.2 Transfer Results

In this section, we will present the transfer results of some of the heterostructures we have built by using the characterization tools introduced in Chapter 2.

Usually, it takes a very long time for the device fabrication. Thus, a comprehensive preliminary inspection of the transfer results is required to prevent the waste of effort and

time. The inspections include checking the defects or damage on graphene, amount PMMA residues, trapped bubbles etc.

3.2.1 Optical Microscopy

After washing away the PMMA film, the heterostructures are first checked under the optical microscope for major defects such as scrolling, peeling, or ripples on graphene. Also, the dark field images revealed the distribution of large bubbles formed within the graphene-MoS_2 interface, as well as some large residues. Figure 3.1 and 3.2 show the results of two transferred graphene on MoS_2 crystal, illuminated in both bright field and dark field microscopy.
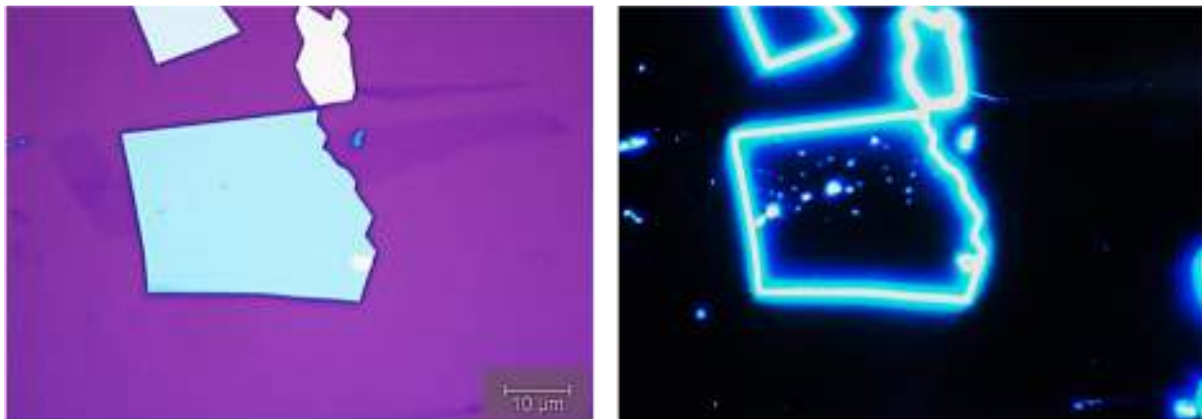

Figure 3.1: Transfer results (T9). Image taken at 100X magnification in (left) bright field and (right) dark field, with 2s exposure.
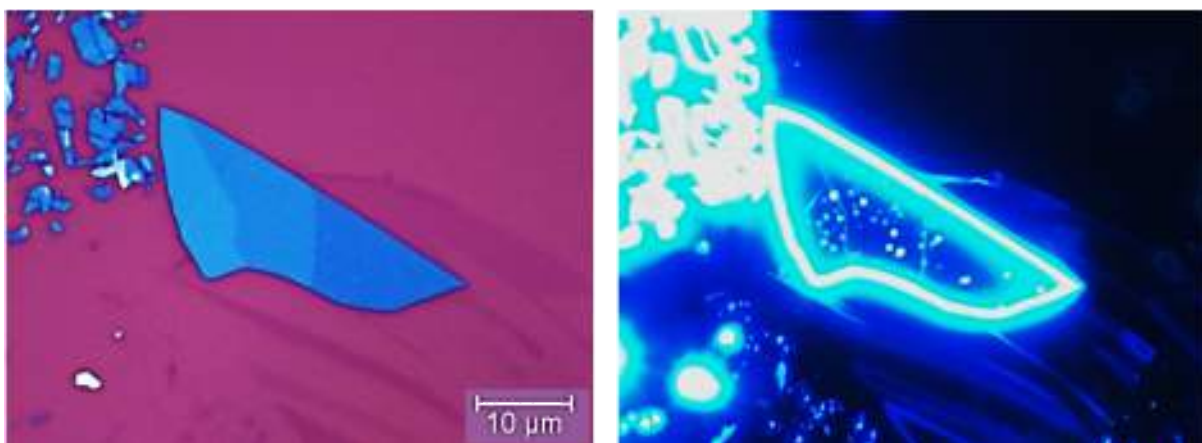

Figure 3.2: Transfer results of (T10). Image taken at 100X magnification in (left) bright field and (right) dark field, with 3s exposure.

3.2.2 Atomic Force Microscopy

Sometimes, the optical microscope is not capable to observe the detail structure on the surface, for example the case that trapped air bubbles are too small to be seen. Therefore, AFM is needed to explore the surface conditions at a smaller scale. In this part, AFM is not only used to investigate the residues and bubbles distribution on the heterostructures, but also determine the roughness of the graphene surface. This is crucial as graphene is a 2D material, its electronic properties, such as the mobility will be greatly affected by the roughness of the surface. Figure 3.3 shows the AFM images of *T9* and *T10* as mentioned in previous part. These are the typical results of most of our transfers. At most of the time, the surface is covered by a high density of PMMA residue or other contaminants. Also, the distribution of trapped air bubbles is relatively homogeneous and the bubbles free regions are not sufficiently large enough for us to fabricate any devices on the heterostructures.
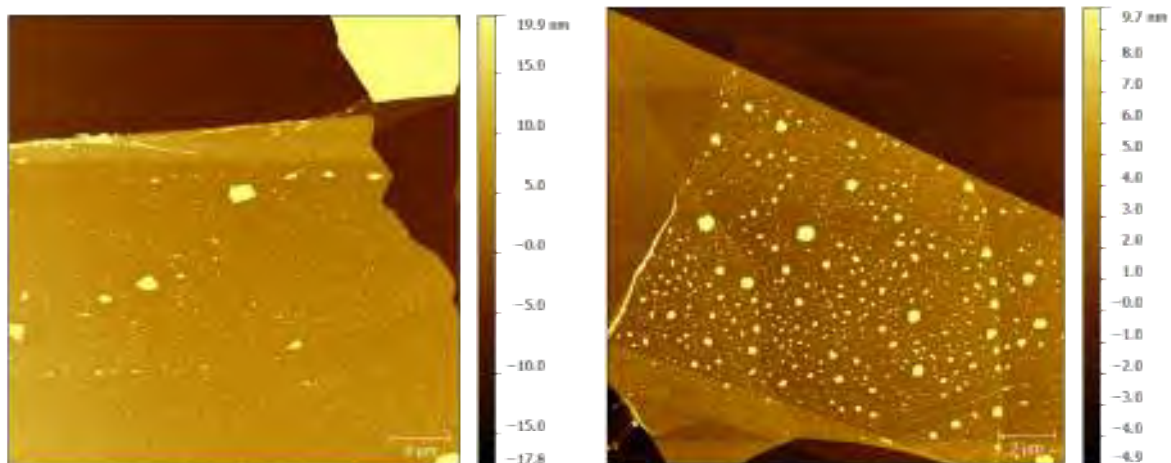
Figure 3.3: AFM results for (left) T9 and (right) T10. Red dotted lines represent the transferred graphene. The bright spots on the surfaces represent the air bubbles and the left over PMMA residue.

i) Bubbles – A self-cleaning mechanism

Just like applying screen protector to our smart phone, air bubbles form because of foreign contaminants being trap within the interface or the film was applied inappropriately. This analogy could use to explain the possible reasons of the bubbles formation in our heterostructures.

First of all, this might due to contamination of flake (either graphene or MoS_2) before transfer, therefore the foreign materials create the height differences on the flat surface thus lead to the formation of air bubbles. Even in the cleanroom environment, this is still inevitable as the flakes will tend to adsorb particles from the air (such as water molecules, hydrocarbons, dust etc.) once they had been prepared. To minimize the amount contaminations, several precautions can be made such as avoid storing the flakes for too long and thermal annealing of the flakes before the transfer. Usually, AFM imaging of the flakes is always done to make sure the cleanliness of the surface before we carry out the transfer process. Other than that, the ways that we attach suspended PMMA film to the substrate wafer are also the reasons for air bubbles to form. However, for the last cause, it can only be improve by a long period of practicing as it is mainly a technical issue.

Nonetheless, the Van der Waals forces within the graphene-MoS_2 interface, attract the adjacent crystals will effectively squeeze out trapped contaminants or force them into the so called "bubble". Based on this argument, we can confidently say that the interface of those bubbles free regions is atomically clean.

ii) Thermal annealing

Despite of the self-cleaning mechanism enable us to obtain atomically clean interface in the graphene-MoS_2 heterostructures, however, in practice those regions are too small for us to have a good use of them. Plus, the surface contaminations such as the PMMA residues are usually high after rinsing with acetone. Therefore, in order to get better quality of heterostructures, a thermal annealing step is introduced. The annealing process is carry out in the inert gas environment (90% Ar, 10% H_2, 0.3L/min) at 300C for 6 hours.

During the thermal annealing, the residues are decomposed and desorb from the surface which are then carry away by the constant air flow. Also, as temperature increases, kinetic energy of the foreign contaminants in trapped in the bubbles will begin to move. Because the interface energy of graphene-MoS_2 interface is much lower compare to the surface energy of MoS_2, the bubbles will tend to coalescing with neighboring bubbles to form a bigger bubble. Therefore, it is expected that the conditions of the heterostructures will improve significantly after thermal annealing process. However, this is not always true, as in some cases, the effect of thermal annealing can be destructive. Figure 3.5 and 3.6 show the improvements of T9 and T10 after annealing, while Figure 3.7 shows a counter example.

Figure 3.5: Result of T9. Images on the left hand side (a,b,c) represent the surface condition before thermal annealing while images on the right hand side (d,e,f) represent the condition after thermal annealing. The roughness of the bubbles free region (evaluated at 1x1μm AFM image c&f) is 0.31nm before annealing while it became 0.09nm after annealing.
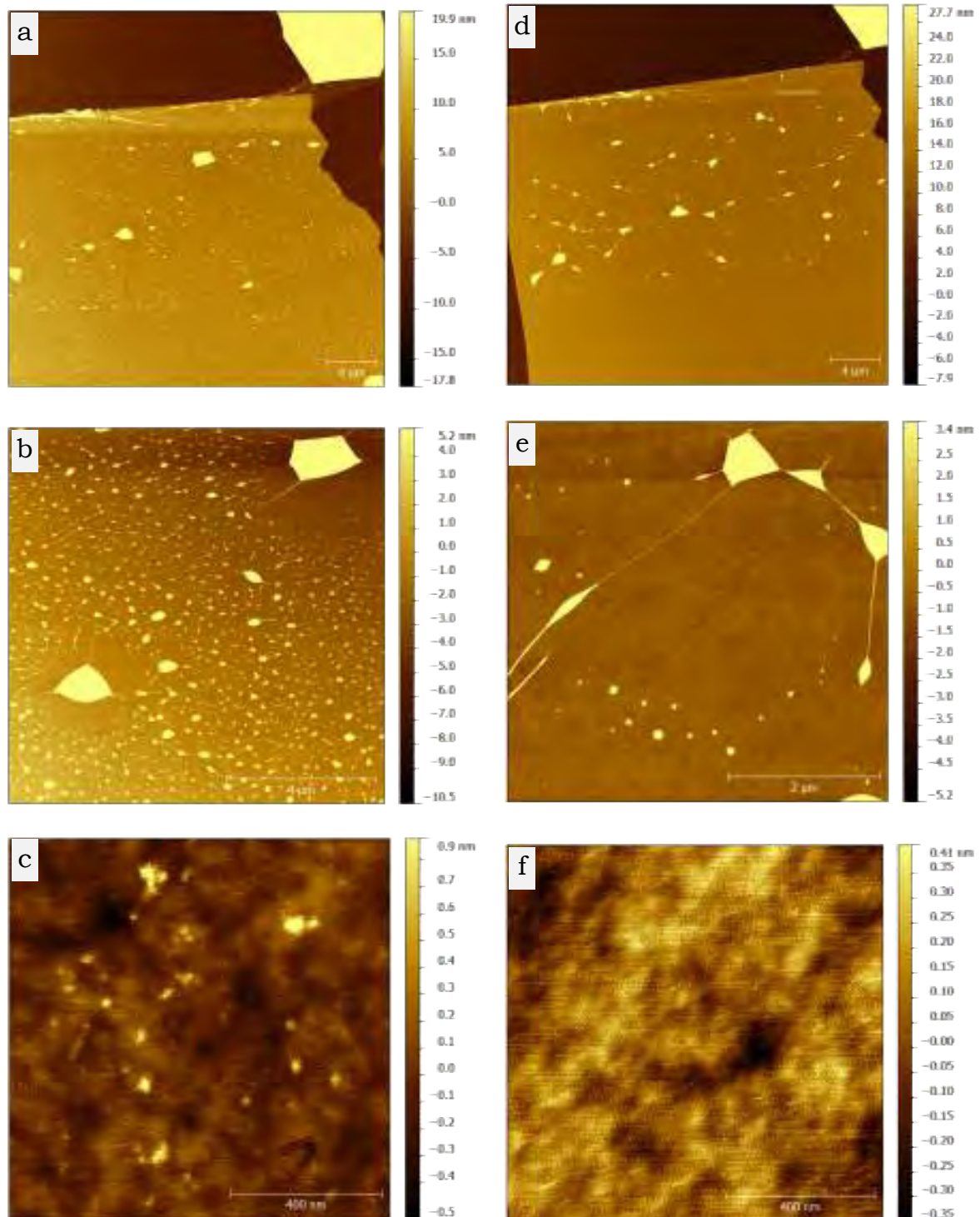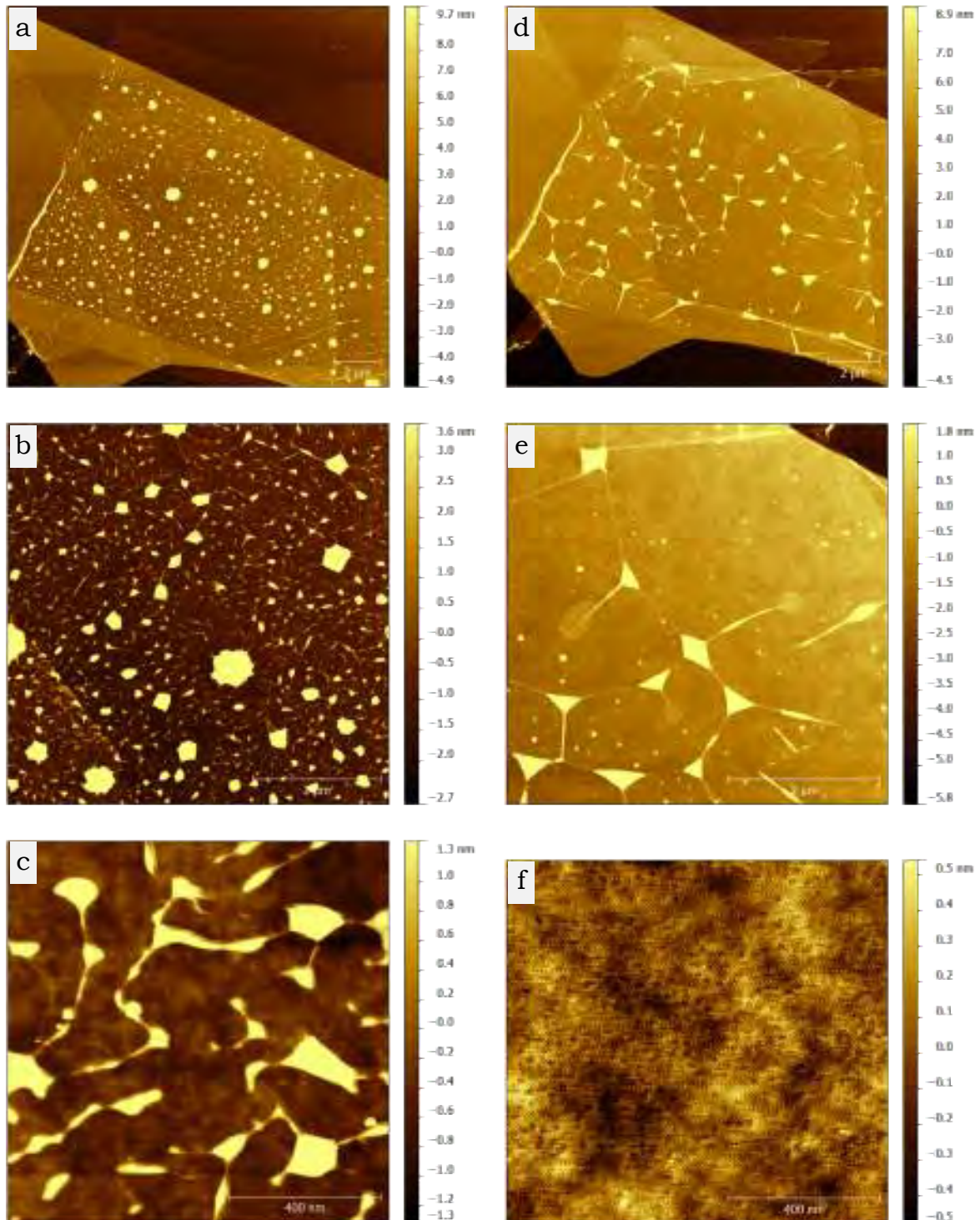
Figure 3.6: Result of T10. Images on the left hand side (a,b,c) represent the surface condition before thermal annealing while images on the right hand side (d,e,f) represent the condition after thermal annealing. The roughness of the bubbles free region is 0.87nm before annealing while it became 0.15nm after annealing.
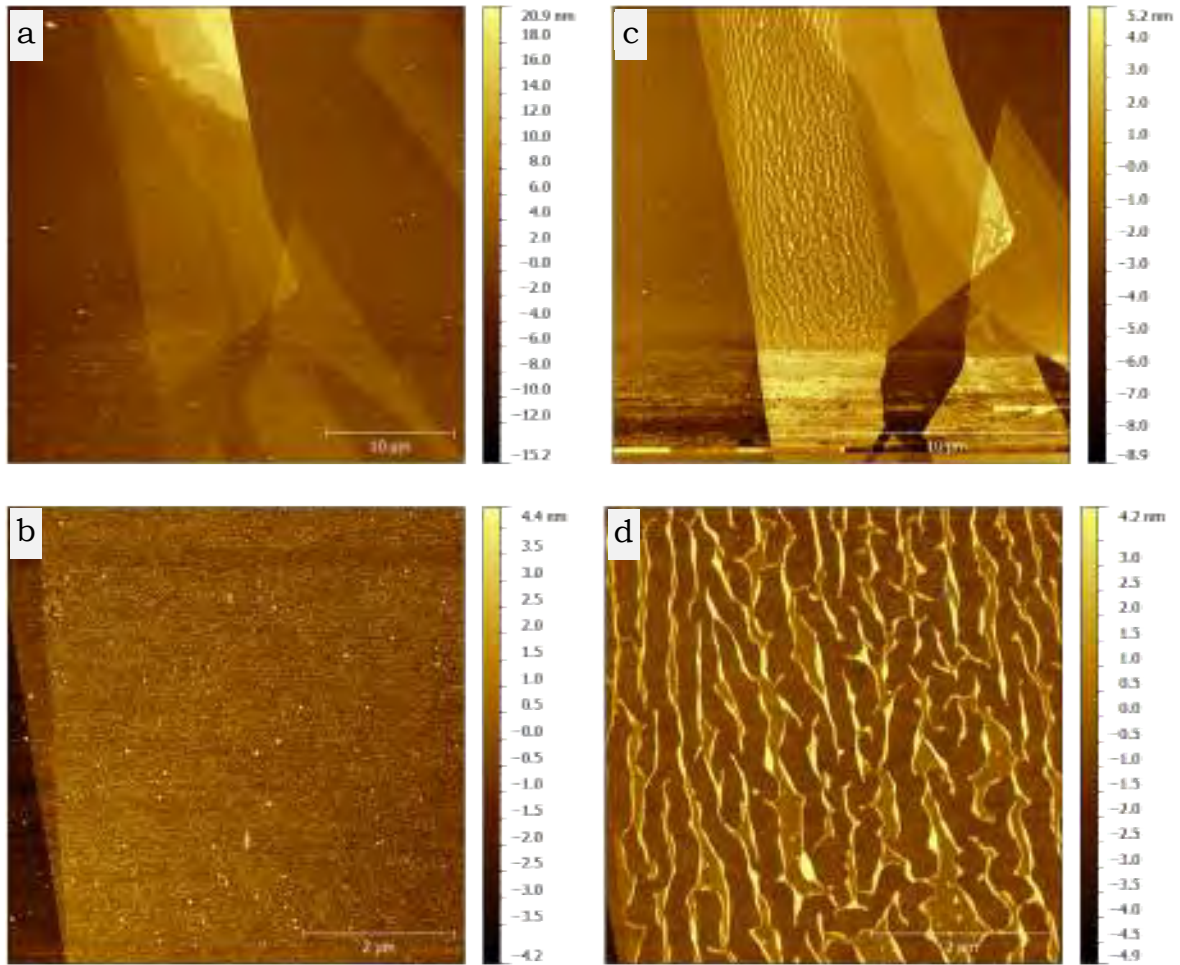
Figure 3.7: Sample destroyed after thermal annealing. Images on the left hand side (a,b,) represent the surface condition before thermal annealing while images on the right hand side (c,d) represent the condition after thermal annealing. The reason is possible due to large amount of tiny air bubbles trapped at the interface. Thus during the thermal annealing, the bubbles movements are too vigorous and causes damages to the transferred graphene.

3.2.4 Raman Spectroscopy

Throughout the transfer process, graphene is mechanically transferred from one substrate to another with the aid of PMMA supporting layer. Ideally, graphene must be put in soft contact with MoS_2 without rubbing and stretching. But in practical, it is still possible to introduce some defects to the graphene flake at the several stages of transfer, and they might not even noticeable via AFM. On the other hand, during the thermal annealing process, the movement of bubbles can be so rapid that may cause graphene to scroll and detach from MoS_2 surface. Also, at high temperature, the Thermal Expansion Coefficient (TEC) mismatch between graphene (negative TEC) and MoS_2 crystals (positive TEC) may results in more defects.

Summing up all the reasons mentioned above, it is necessary for us to perform Raman spectroscopy on the transferred and annealed graphene sample, to ensure the quality of transferred graphene is preserved.
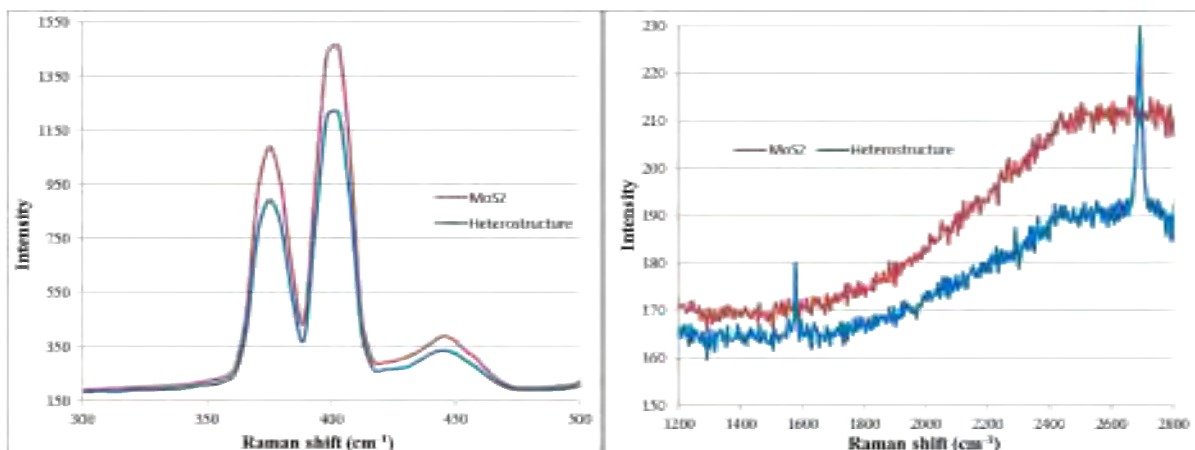

Figure 3.7: Raman spectrums of MoS_2 substrate (blue) and graphene-MoS_2 heterostructures.

Normally, Raman spectroscopy is applied to several positions on the heterostructures to check for the existence of D peak. The spectrum of heterostructures generally inherits the spectrum of MoS_2, except that the peaks from graphene are also present.

3.3* Heterostructures involved CVD MoS$_2$

In this part, instead of using mechanical exfoliated, few-layers MoS$_2$ flake, we will try to use the monolayer CVD MoS$_2$ as part of the heterostructures. This is because monolayer MoS$_2$ exhibit interesting properties that is absent from few-layer MoS$_2$. It is very unlikely to obtain monolayer MoS$_2$ via the mechanical exfoliation, thus in order for heterostructures to have more practical value, benefits of CVD film will eventually outweigh the exfoliated flakes when it comes to real life applications. The properties of both monolayer CVD MoS$_2$ and natural exfoliated monolayer MoS$_2$ are mainly similar to each other. There are indeed some differences, such as the texture, intrinsic properties which become the research interest of many scientists in the material science area.

Based on reasons mentioned above, we think that it is a good idea to create a heterostructures based on the CVD MoS$_2$. However, as both graphene and monolayer CVD MoS$_2$ are too thin, and the texture of the heterostructures will be sensitive to the rough SiO$_2$ surface. Therefore, the heterostructures will be encapsulated with a relatively thicker hexagonal-Boron Nitride crystal (hBN). To achieve such configuration, one dry transfer and one wet transfer are required.
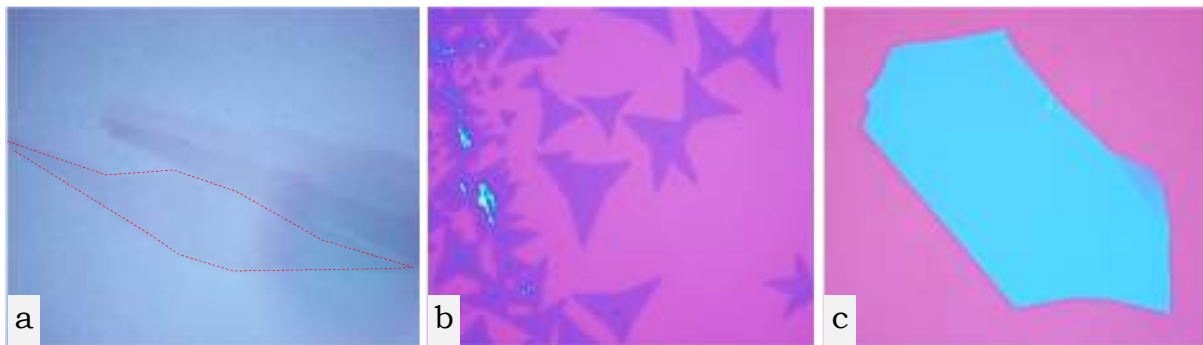

Figure 3.8: (a) Graphene, (b) Typical monolayer CVD MoS$_2$ and (c) hBN

The procedures are carried out as follow:

i) A dry transfer is performed to transfer graphene onto the monolayer CVD MoS$_2$.

Figure 3.9: After dry transfer of graphene.

ii) The wafer is then spin-coated with PMMA, and then followed by the wet transfer as discussed in section 3.1.2.The entire heterostructures is transferred onto hBN substrate.
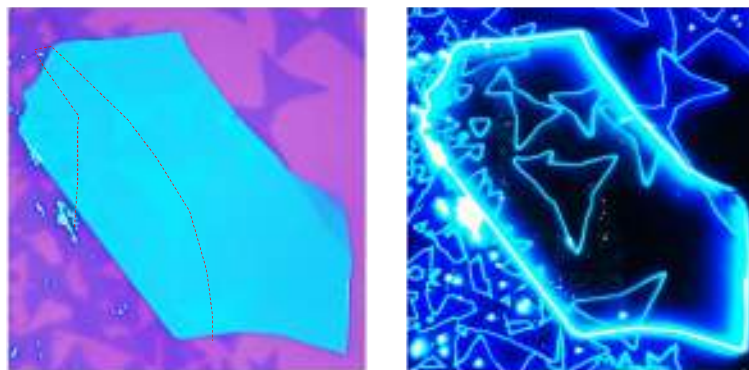
Figure 3.10: Results after wet transfer of graphene-MoS$_2$ heterostructure to hBN substrate.

iii) Finally, PMMA is washed away, and subsequently the thermal annealing.

Figure 3.11: Results after thermal annealing.

The AFM results of the heterostructures before and after thermal annealing are shown in the following figures:

Figure 3.12: Images on the left hand side (a,b) represent the surface condition before thermal annealing while images on the right hand side (c,d) represent the condition after thermal annealing.

It is once again show that thermal annealing can effectively increase the bubbles free region of our transferred sample and reduce the residues. However, for very thin films, the ef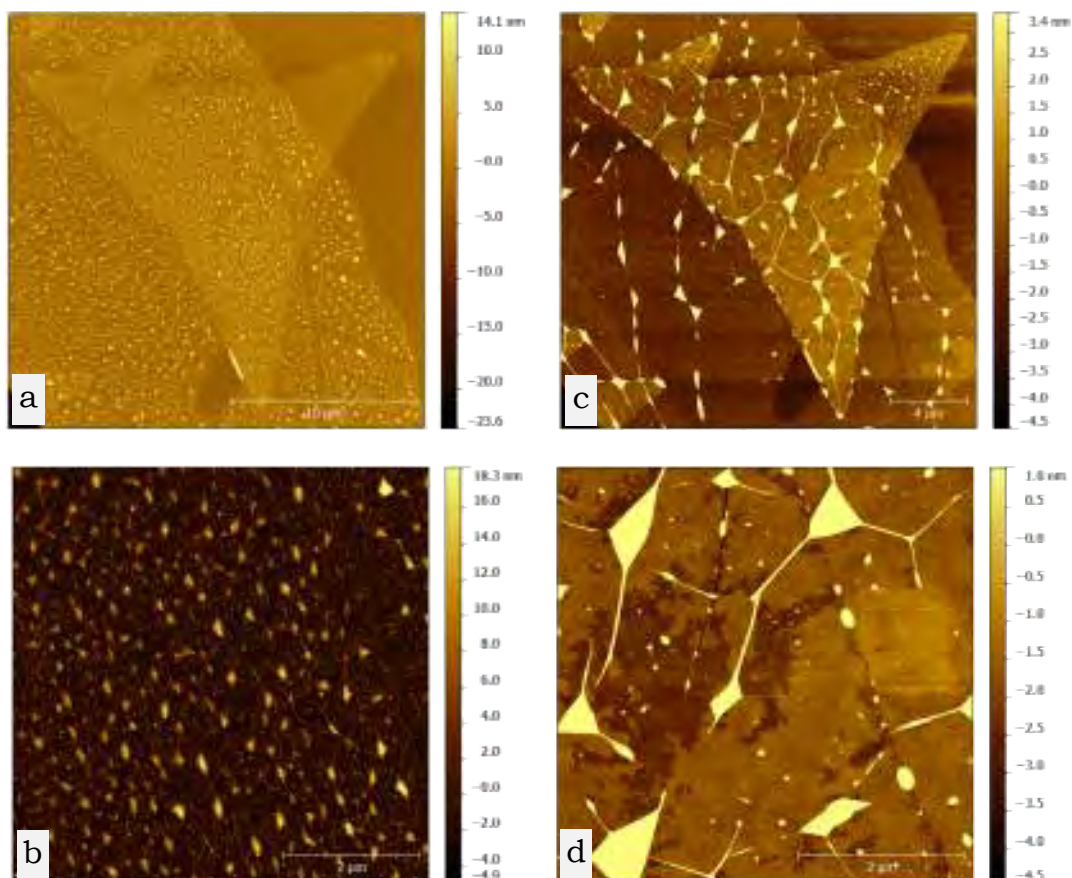fect of thermal annealing can be destructive if the heterostructures is not encapsulated by a flat surface (in our case, hBN). We created another graphene-CVD MoS_2 heterostructures without hBN encapsulation (that is, on SiO_2 surface), and we found that the entire structure was almost spoilt after thermal annealing. The reason is unclear, but based on our experience, it is observed that graphene transferred onto a rough surface tend to detached and creased after thermal annealing.
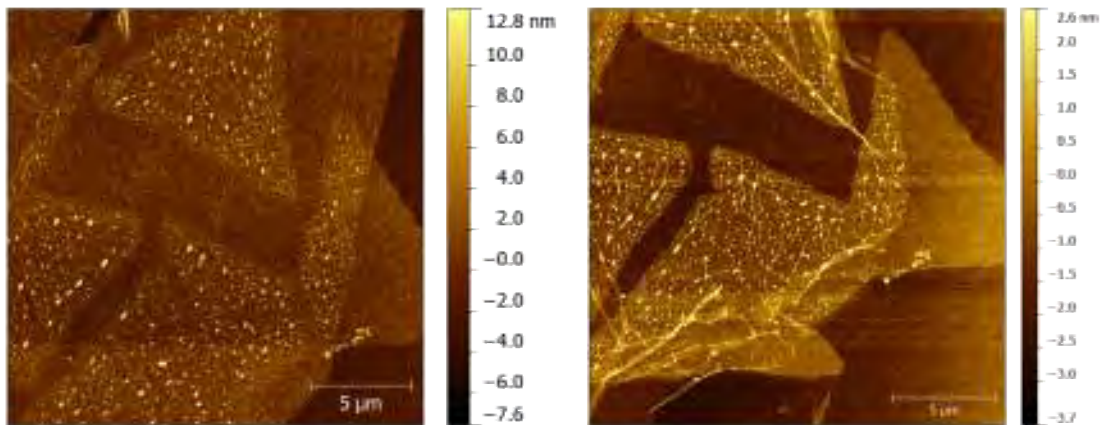

Figure 3.13: Thin heterostructures without encapsulation before annealing (left) and after annealing (right). It can be seen that graphene is detached from MoS_2 surface while bubbles density is still remain high.

3.4 Challenges and Precautions

Transfer techniques, conceptually it is a simple and requires only basic facilities such as a microscope and micromanipulator. However, in practice, it takes months to master the techniques. Over the past 7 months of attempts, we have done more than 50 transfers and only a few of them are suitable for device fabrication.

The first challenge would be getting the flakes that are suitable for transfer. As we used mechanical exfoliation to obtain graphene and MoS_2, which is a low yield process and the outcomes are nearly unpredictable. For transfer, it is preferable to have an isolated flakes that is not attach to other flakes with different thickness, bigger in size and clean from contaminants. Unlike CVD film, the only way to get a nice sample is keep on exfoliating.

Next, the biggest challenge in this project is to align the flakes during transfer. Usually, the flakes involved in transfer are at the size of 10μm or less. With no help from other sophisticated instruments but a hand controlled micromanipulator and a microscope, getting the flake align in the desire angle and direction is exceptionally difficult. Other than the alignment, vibration from the surrounding is also a big issue as the flakes are so small, thus a little vibration will easily lead to huge misalignment and failures.

On the other hand, the samples we are handling (graphene and thin-MoS_2 flake) are very sensitive, which required us to be more careful during the process. Else, it would result in damages on the samples. This limitation makes the transfer become more challenging.

Lastly, because we have to work at a tiny scale, there are many expected and unexpected difficulties that one might encounter. Thus, practices and experiences are the key to carry out a good transfer. Currently, we are still on the way to optimize our transfer techniques as well as the equipment, and hopefully in the near future, the quality of the transferred sample will be getting better and better.

Chapter 4 Charge Transport in Graphene

In this chapter, we will discuss the experimental realizations of the charge transport properties as well as the procedure of device fabrications.

4.1 Experiment Techniques

4.1.1 Device Geometry

Usually, the common device geometry for performing electrical measurements on graphene samples is the Hall bar, shown in Figure 4.1.
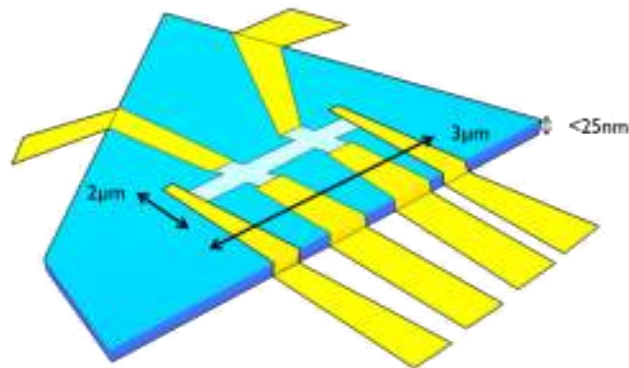

Figure 4.1: Schematic diagram of a typical Hall bar device.

4.1.2 Modulation of Carrier Density in Graphene

In this project, graphene will be transferred onto a thin multilayer MoS_2 and the entire heterostructures sit on a heavily doped silicon wafer, capped with an insulating silicon oxide layer with thickness equal to 300nm.
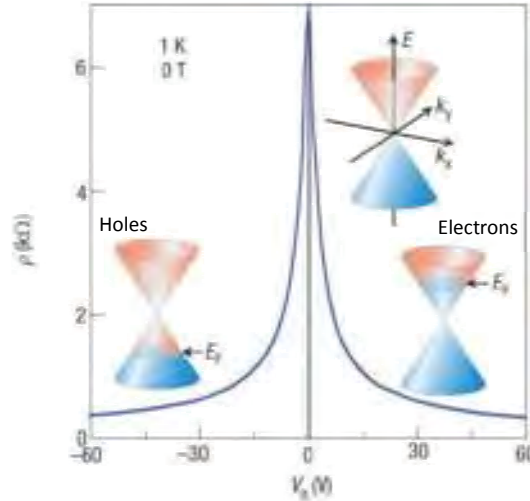
Figure 4.2: Modulation of the resistivity (carrier density) of graphene sample by the application of back gate voltage, V_g. Maximum point at V_g=0 represent the Dirac point.

By applying a back gate voltage (V_g) to the silicon substrate, the Fermi level (E_F) of graphene can be tuned, so as the carrier density. In Figure 4.2, as E_F approaches the Dirac point, the number of available carrier decreases, and hence resulted in a higher resistivity. This ambipolar nature of graphene enables the study of electron transport when E_F is above the Dirac point (in the conduction band) and hole transport when E_F is below the Dirac point (in the valence band).

As shown in Figure 4.2, the $\rho(V_g)$ curve is symmetric about the Dirac point at V_g=0 for intrinsic graphene. However, in practice, the location of Dirac point usually drifted away from V_g=0 due to the doping of the graphene sample. The "dopants" are usually contaminants such as dust or water molecules, and the Dirac point can be brought back closer to V_g=0 by removing the contaminants from the sample surface. Furthermore, thermal excitation, the presence of charged impurities, ripples in the graphene sheets will also prevent the charge carrier density from going down to zero at the Dirac point.

4.1.3 Mobility and Density of Carriers

From the Hall bar geometry, one can easily evaluate the mobility of the graphene in the heterostructures by using a four-point measurement.
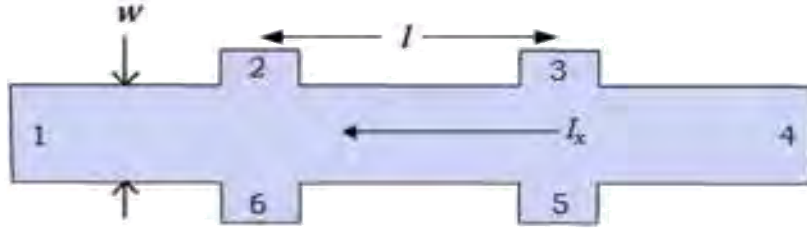
Figure 4.3: 6-probes Hall bar device

A current (I) is driven across electrode 1 and 2, by measuring the voltage drop between probe 6 and 5 (V_{23}) or V_{65}, the resistivity of the graphene sample is then defined as:

$$\rho_{xx} = \left(\frac{w}{l}\right)\left(\frac{V_{23}}{I_x}\right) \tag{4.1}$$

which ρ_{xx} has units of Ohms (Ω), w is the width and l is the length of the graphene channel between the voltage probes.

From the Drude model, the conductivity σ is defined to be:

$$\sigma = \rho^{-1} = ne\mu \tag{4.2}$$

where n and μ are the carrier density and mobility ($cm^2V^{-1}s^{-1}$), and they can generally be determined from either field effect or Hall effect measurements during the experiments.

i) Hall Effect approach

In the presence of a transverse magnetic field B_z, electron with current density j_x experience a Lorentz force equal to $-e\vec{v} \times \vec{B}$. In equilibrium, this system is balanced by the Hall electric field $\vec{E}_H = R_H\vec{B} \times \vec{j}$, where R_H is called the Hall coefficient, which is defined as:

$$R_H = \frac{E_H}{B_z j_x} = \frac{1}{ne} \tag{4.3}$$

The Hall coefficient therefore depends only on the density of carriers, n an intrinsic material property. Substituting $E_H = V_y w$ and $j_x = I_x/wt$, the expression of Hall coefficient become:

$$R_H = -\frac{1}{ne} = \frac{V_y t}{I_x B_z} \tag{4.4}$$

where V_y is the voltage drop perpendicular to the current flow I_x (that is, in Figure 4.3, V_y can be either V_{26} or V_{35}. In the above equation, t represent the thickness of the sample. However in a 2D system, t is meaning less therefore which is always omitted. Therefore, the 2D carrier density has units of cm^{-2} instead of cm^{-3} in bulk material. Finally, we arrive at

$$\rho_{xy} = R_H B_z \tag{4.5a}$$

$$n = -\frac{B_z}{e\rho_{xy}} \tag{4.5b}$$

where $R_{xy} = V_y/I_x$ and $\rho_{xy} = V_y/I_x$ are the Hall resistance and resistivity respectively, and they are identical in 2D systems. Once the carrier density is known, the Hall mobility μ_H can simply be calculated from equation (4.2).

ii) Field Effect approach

Normally, during the measurements, the graphene sample in the heterostructures is grounded, while a back gate voltage V_g is applied at the Si substrate.
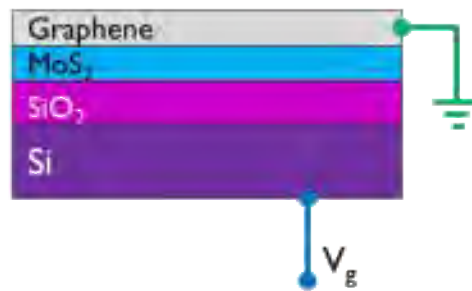

Figure 4.4: Schematic of vertical cross-section of graphene-MoS$_2$ heterostructures

As the thickness of MoS$_2$ flake (<10nm) is usually much smaller than the thickness of gate oxide thickness (~300nm), we assume that the capacitance contribution from MoS$_2$ is negligible. Therefore, in the system shown in Figure 4.4, we have the gate capacitance:

$$C_g = \frac{\varepsilon_0 \varepsilon_r}{t_0} \tag{4.6}$$

where ε_r and t_0 are the relative dielectric constant and thickness of the SiO$_2$ layer, and ε_0 be the permittivity of free space. Hence, the density of carriers in graphene sample (n) can be estimated from the surface charge density induced by the application of a gate voltage (V_g):

$$n = \frac{C_g V_g}{e} = \frac{\varepsilon_0 \varepsilon_r V_g}{t_0 e} \tag{4.7}$$

As *n*=0 at the Dirac point, any doping of the sample is compensated for by replacing V_g in the above equation by (V_g-V_{gD}) with V_{gD} the gate voltage at the Dirac point.

By using this model, it was shown (Zhang et al., 2005) that the induced carrier densities estimated using Equation (4.7) having good agreement with the results determined from Hall effect measurement (i.e. via Equation (4.5)). However, this estimation is usually based on graphene alone and it may not be valid for the case of graphene-MoS$_2$ heterostructure. It is because the electron interaction between graphene and MoS$_2$ is not considered in this model. More preciesely, the carrier desity obtained by this model are the sum of carrier densities of both graphene and MoS$_2$. That is:

$$\frac{C_g V_g}{e} = n_{graphene} + n_{MoS_2} = n_{total} \tag{4.8}$$

Finally, the field effect mobility μ_{FE} can be simply extracted from the gate voltage dependence of conductivity:

$$\mu_{FE} = \frac{d\sigma}{dV_g} \frac{1}{C_g} \tag{4.9}$$

where σ is the conductivity of the sample and C_g is the gate capacitance which is evaluated as $C_g = ne/(V_g - V_{gD})$ if doping effect is observed.

4.2 Device Fabrication

In this section, we will briefly describe the procedure of device fabrication. During the fabrication the graphene sheet in the heterostructures will be patterning into the Hall bar geometry.

In practical, the size of our heterostructures is usually around 10μm. In order to pattern the graphene and make it into a working device with electrical contacts, the use of Electron Beam Lithography (EBL) is required. Comparing to laser writer, EBL deliver higher resolution, and which is essential for well-defined electrodes as well as the etching region.

Figure 4.5: A typical 8-probes device with Hall bar geometry.

i) Polymer spin-coating

To begin with this process, an EBL polymer resist Poly-methyl-methacrylate (PMMA) is first spin-coated onto the sample (in this case, a graphene sheet).

ii) Electron Beam Patterning

Inside the EBL chamber, certain areas will be exposed with highly accelerated electrons according to the pattern we defined through the computer program. As a result, the polymer chains in the exposed PMMA regions will break, which will then be removed during the development process.
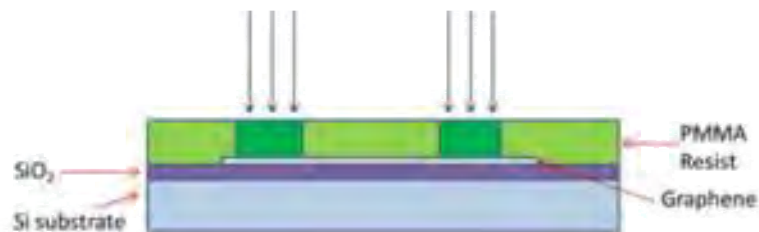
iii) Development

The exposed PMMA can be removed with a mixture of Methyl-isobutyl-ketone (MIBK) and isopropanol (IPA) solution because of its broken polymer chains. On the other hand, in the unexposed region, PMMA will remain intact and it will act as a mask for subsequent steps, such as the deposition or etching.

iv) Thermal Evaporation

As required for electrical measurements, metal contacts and electrodes are deposited via the thermal evaporation. This is done by EBL patterning of the location of the contacts, and the metal is then precisely deposited on the regions where PMMA was removed during development.

v) Lift-off Process

After metal was evaporated on the sample, a lift-off process is done to remove the PMMA film and excess metal. This is achieved by submerge the sample in 60^0C acetone for at least an hour.

vi) Etching

Finally, the graphene is etched into the Hall bar geometry via the oxygen plasma etching. To do so, the sample is again spin-coated with PMMA, and an etch mask is defined by EBL. After development, the sample is put into the plasma chamber, and only the region covered by PMMA etching mask is protected and remained intact after the process.

4.3 Results and Discussion

As part of the characterization, we will perform electrical measurements on the graphene-MoS$_2$ heterostructures built in Chapter 3, and investigate the electronic behaviour of graphene in the heterostructures. Unfortunately, due to the time constrain, we are not able to present the results of the heterostructures made of CVD MoS$_2$ (Section 3.3) at this moment.

4.3.1 Fabrications

After the transfer process, a clean, bubble free region on the heterostructures is selected for the device fabrication. In the case of T10 as mentioned in Chapter 3, two regions are chosen and two 6-probes Hall bar device were fabricated. During the fabrication process, PMMA is repeatedly spin-coated and removed on the heterostructures. Thus, additional thermal annealing processes were done to ensure the surface cleanliness of the devices.
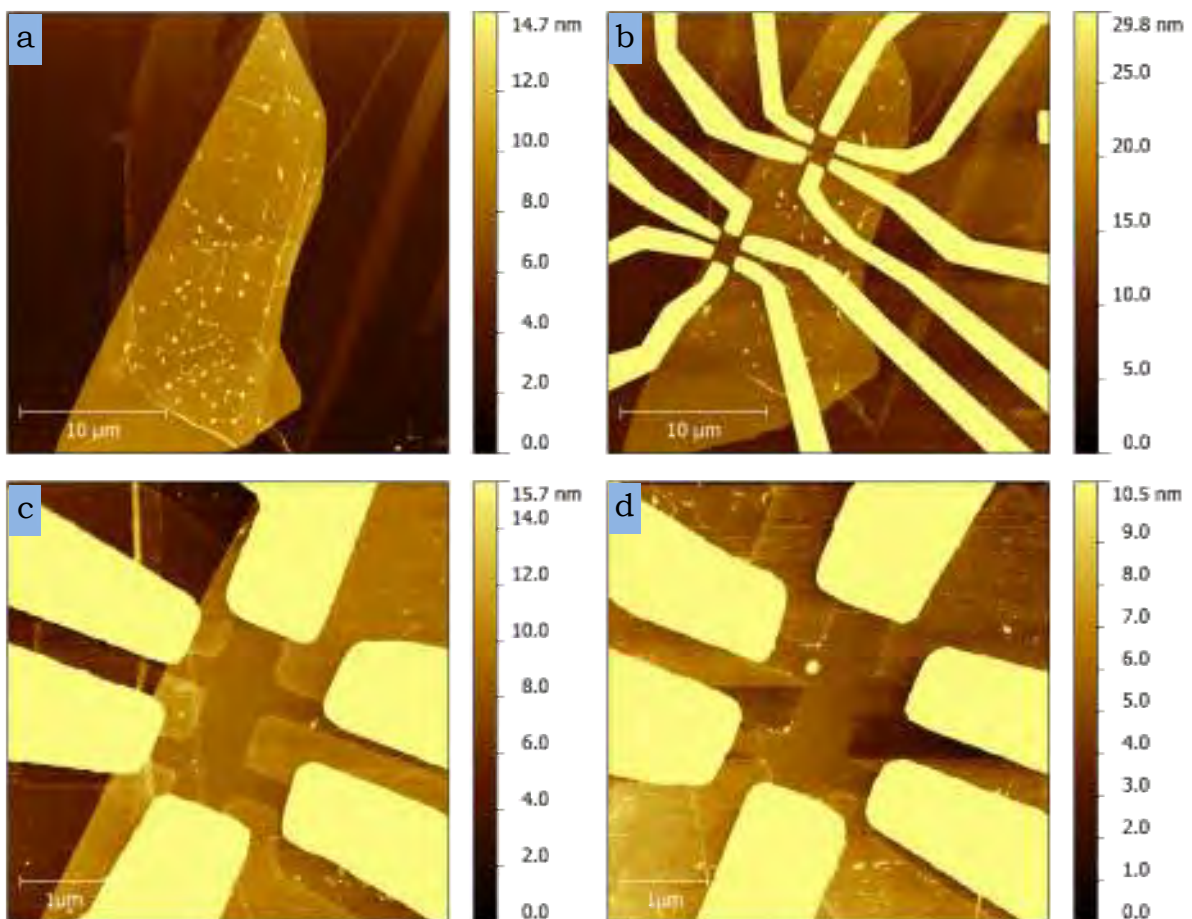

Figure 4.6: Device fabrication of T10. AFM topography of (a) the heterostructures after transfer, (b) the heterostructures with two Hall bar devices fabricated, and (c,d) the devices.

4.3.2 Electrical Measurements

In order to extract the electronic profile of the devices, the dependence of the resistance versus the back gate voltage V_g applied to the Si substrate is measured. Figure 4.7 show the photos of the devices fabricated in previous section, with the electrode labelled.
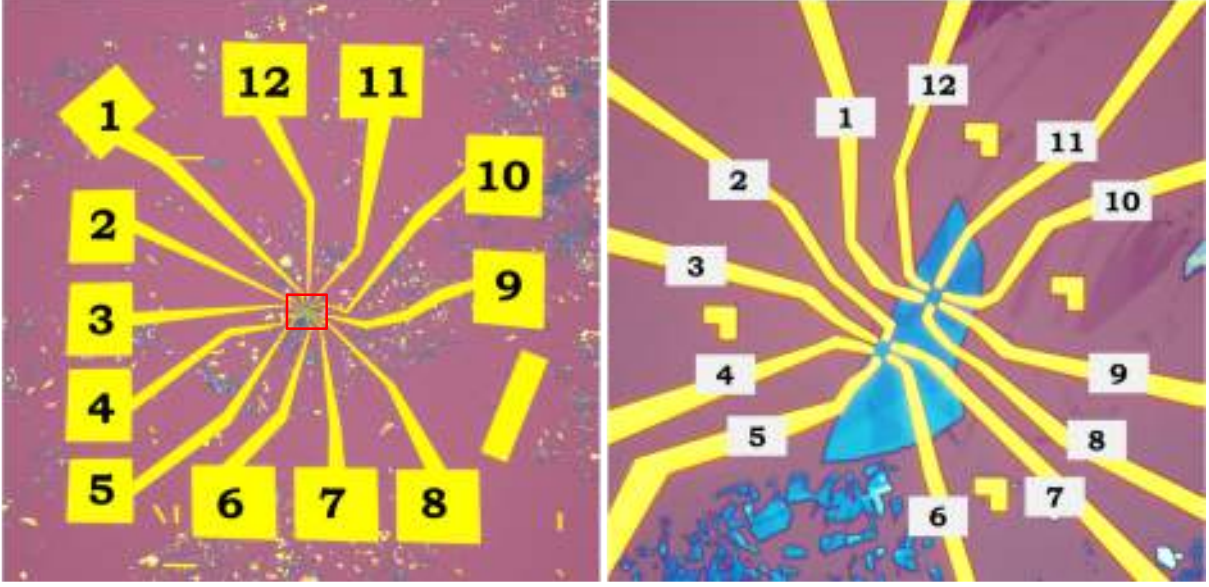

Figure 4.7: Two independent devices fabricated on graphene-MoS$_2$ heterostructures.

The measurement is taken at 4.2K, and a magnetic field (B) perpendicular to the devices is applied during the measurement. At each V_g and B, current (I_{52}) is sent from contact 5 to contact 2, while the potential difference between electrodes 6 & 7 (i.e. the longitudinal voltage, V_{67}) and electrodes 6 & 4 (i.e. the transverse voltage, V_{64}) are recorded at the same time. The value of V_g is varying from -40V to 50V while the magnetic field B is varying from 0T to 4T. Similar procedure applies to the other device as well.

After the measurements, the magneto resistivity, $V_M(V_g, B)$ is calculated by Equation (4.1), with $w/l = 0.7$ obtained from Figure 4.6 (c) and the Hall resistivity, $V_H(V_g, B)$ are calculated by dividing V_{64} to I_{52}. The results are shown in the following contour plots. Besides, a plot of each resistivity and conductivity at zero magnetic field are shown in Figure 4.10.
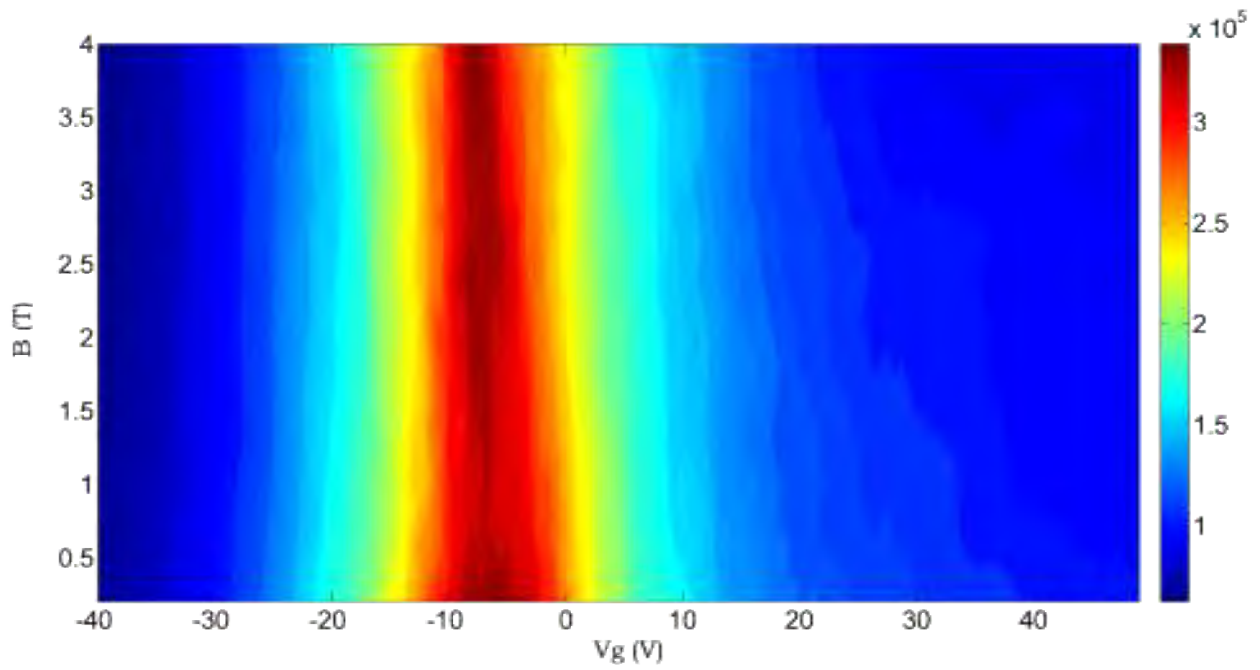
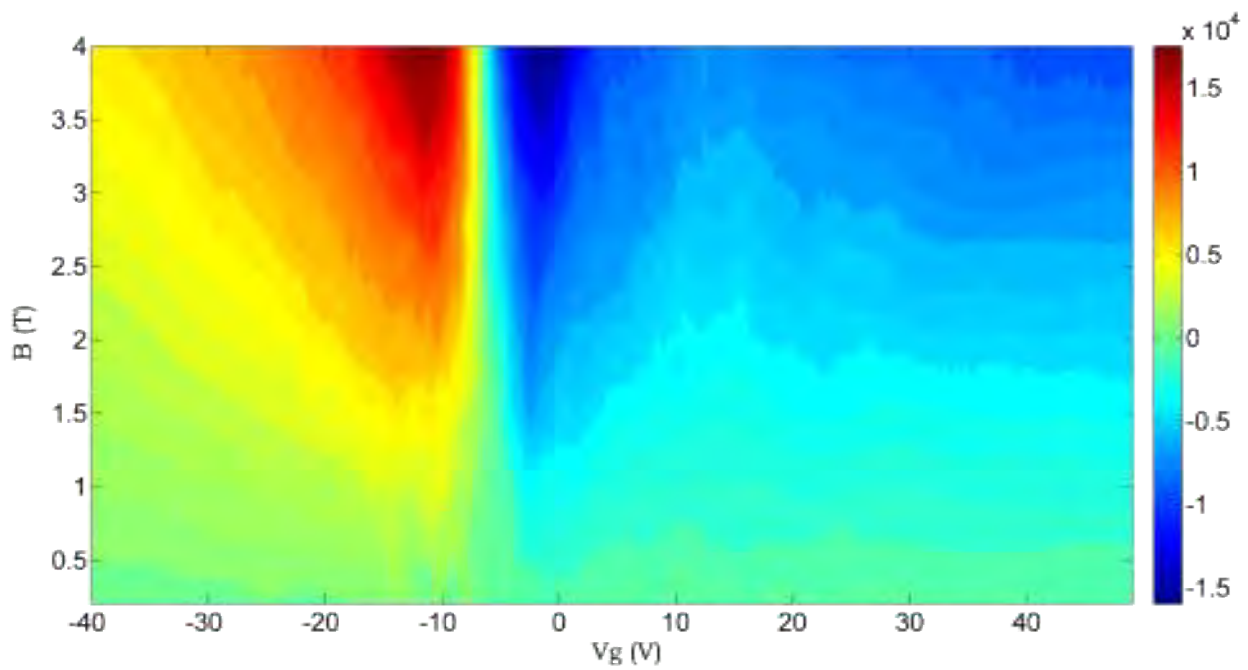Figure 4.8: Contour plot of magneto resistivity, ρ_{xx}.

Figure 4.9: Contour plot Hall resistivity, ρ_{xy}, which indeed clearly shows that Hall resistivity
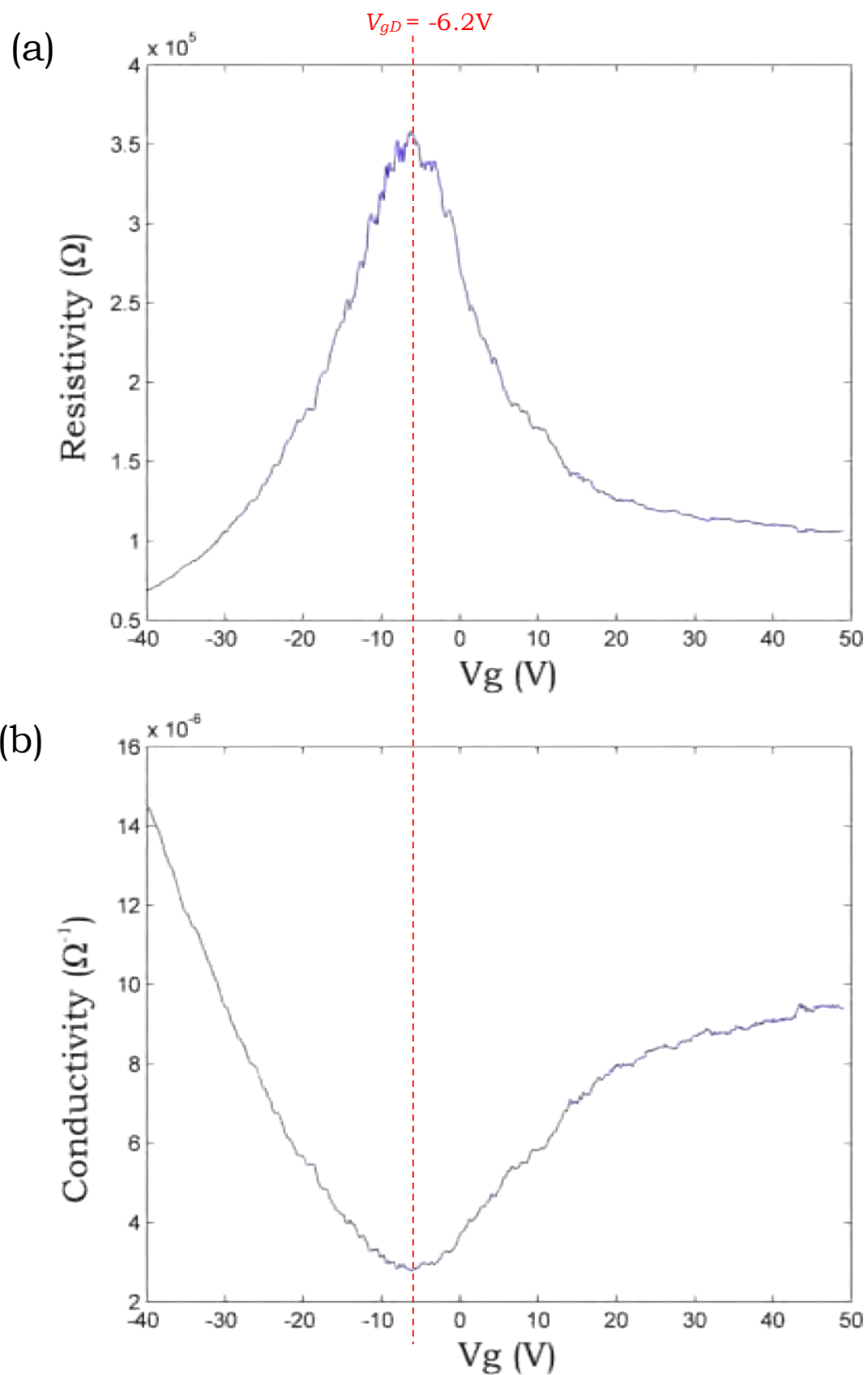
vanish when B approaches zero.

Figure 4.10: Variation of (a) resistivity, ρ_{xx} and (b) conductivity, ρ_{xx}^{-1} with respect to V_g at zero magnetic field ($B=0$). The red dotted line represents the charge neutrality point.

From Figure 4.10, the conductivity (resistivity) reaches a minimum (maximum) at V_{gD}=-6.2V, which is identified as the charge neutrality in the graphene sheet (i.e. The Dirac Point). For $V_g < V_{gD}$, conductivity decreases as V_g increases, indicating holes are populated the heterostructures. On the other hand for $V_g > V_{gD}$, electrons start to populate the heterostructures, and hence the conductivity is also increases. For graphene alone, as described by the ambipolar behaviour, the resistivity (or conductivity) profile is symmetric about the charge neutrality point (Figure 4.2). However, surprisingly for graphene-MoS_2 heterostructures, it is noticed that the symmetry is lost at some $V_g=V_T$ (V_g~15V particular in this case) and the conductivity begins to saturate as V_g increases beyond V_T.

In order to calculate the carrier density in graphene, the values of Hall coefficient, R_H at each V_g is extracted from the Hall resistivity results in Figure 4.9, by using equation (4.5a). Hence by Equation (4.5b), the carrier density at each V_g is evaluated and shown in Figure 4.11.
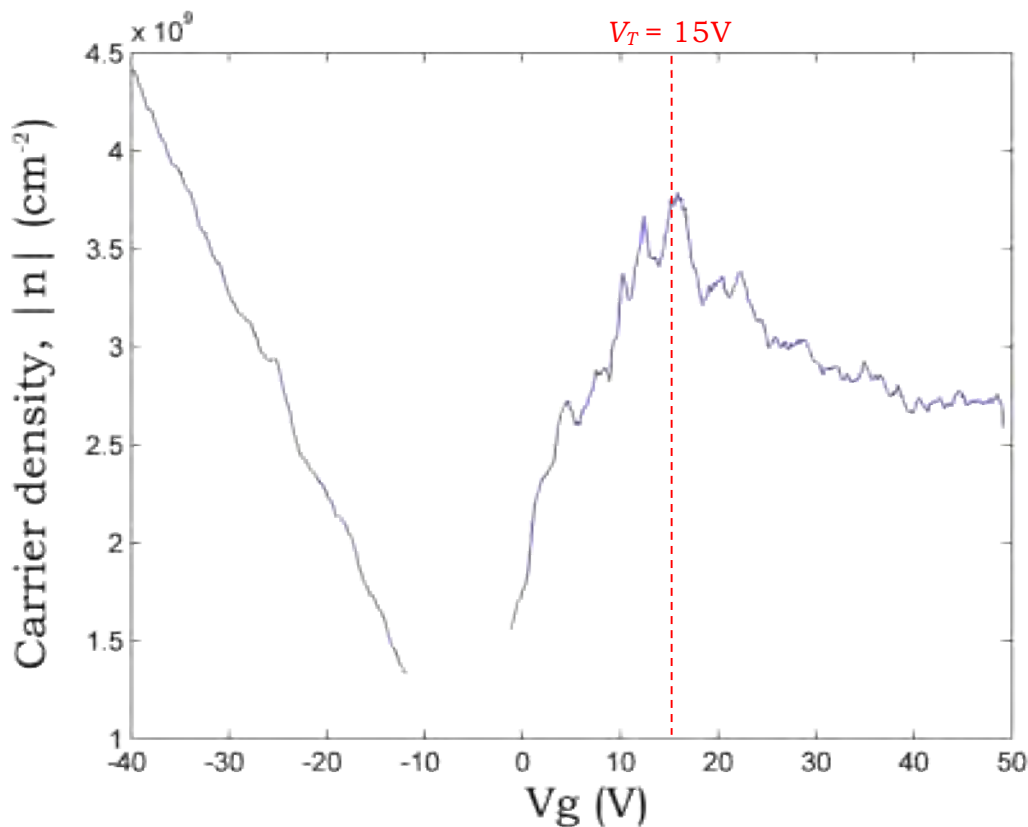

Figure 4.11: Carrier density of graphene, n_g in the heterostructures at each V_g.

It is also observed that the carrier density in graphene decreases as the saturation begins at $V_g=V_T$=15V. Finally, by equation (4.2) and results in Figure 4.10, the Hall mobility of the heterostructures before saturation is found to be 20,500 $cm^2V^{-1}s^{-1}$.

Regarding the drop of carrier density in graphene observed in Figure 4.11, according to Larentis et al. (2014), which can be illustrated by using the band structure diagrams as shown in Figure 4.12.
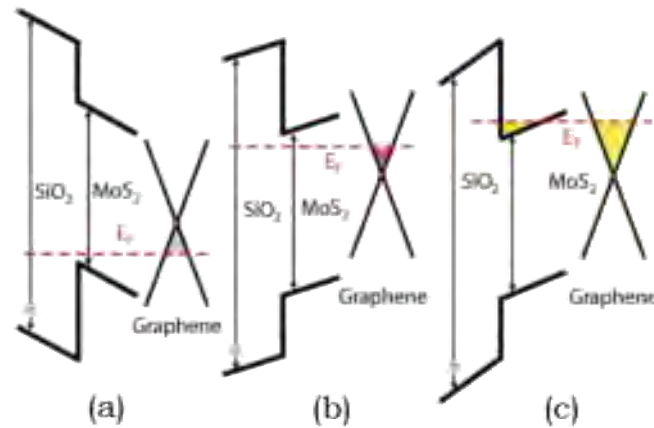

Figure 4.12: Band diagrams of the graphene-MoS$_2$ heterostructures for (a) $V_g<V_{gD}$, (b) $V_{gD}<V_g<V_T$, and (c) $V_g>V_T$ when electrons are induced in the MoS$_2$ conduction band.

From the figure, for $V_g<V_{gD}$ ($V_g<V_{gD}<V_T$), gate-induced holes (electrons) are injected to the graphene valence band (conduction band). For $V_g<V_T$, the Fermi level in graphene is lower than the MoS$_2$ conduction band edge. Hence, if a sufficiently large gate bias is applied, in order to achieve the equilibrium, the MoS$_2$ conduction band will bend and aligned with graphene Fermi level. Thus, the gate-induced carriers at $V_g>V_T$ (in this case, electrons) begin to populate MoS$_2$ conduction band and hence a drop in graphene carrier density is expected as V_g go beyond V_T.

On the other hand, from the Field effect approach, the total carrier density estimate by Equation (4.8), the total carrier density, n_{total} is linearly increasing for $V_g>V_T>V_{gD}$. Therefore, more and more electrons are populated in MoS$_2$ instead of graphene. Hence, the conductivity begins to saturate as the mobility is lower in MoS$_2$ than in graphene.

Finally, it is also noticed that the mobility of graphene layer encapsulated by MoS$_2$ (in this case $\mu=20,500$ cm^{2}V^{-1}s^{-1}) is much lower as compared to the mobility of graphene layer encapsulated by hBN ($\mu\sim100,000$ cm^{2}V^{-1}s^{-1}).

Chapter 5 Conclusion

5.1 Summary of the results

In summary, graphene-MoS$_2$ heterostructures are built via the dry transfer technique and characterized by using tools such the optical microscopy, AFM and Raman spectroscopy. Also, the electrical properties and the carrier distribution of the graphene layer in the heterostructures are investigated. It is observed that the conductivity of graphene layer in the heterostructures saturate at certain back gate voltage, V_g on the electron branch. Furthermore, from the Hall effect study, the carrier density of graphene layer is evaluated and the decrease in carrier density is revealed at the saturation region. This could be associated with the onset of MoS$_2$ conduction band population.

In term of mobility, the quality of the graphene-MoS$_2$ heterostructures fabricated in throughout this project is not considered great, and the reasons may due to the roughness of the MoS$_2$ flake we used during the fabrications. In our graphene-MoS$_2$ heterostructures, the roughness of the MoS$_2$ flake is 0.15nm and the resulted graphene mobility is found to be 20500cm^{2}V^{-1}s^{-1}. It known that the average mobility of graphene sheet deposited on a typical SiO$_2$ surface (with roughness ~ 0.18nm) is about 15,000cm^{2}V^{-1}s^{-1}. Therefore, we believe that the roughness of the substrate is one of the main limiting factors in this case.

Finally, the results obtained from our graphene-MoS$_2$ heterostructures show a very good agreement with the very recent findings reported by Larentis et al. in early 2014. Therefore, in conclusion, we have successfully fabricated a graphene-MoS$_2$ heterostructures, with an atomically clean interface and the interactions between these two materials are observed.

5.2 Future studies

With the current result we obtained from throughout the project, the graphene-MoS_2 heterostructures indeed exhibit a few interesting properties, such as the saturation of conductivity. Nonetheless, due to the time constrain, we cannot fully explore its characteristic in more details. As a continuation of this project, a few suggestions are proposed and listed below:

1) Studies on spintronics

Both graphene and MoS_2 exhibit the properties that are highly favoured in the study of spintronics. With a good graphene-MoS_2 heterostructures, more researches and experiments regarding the spin transport can be carry out and reveal potential applications of this hybrid materials in future technology.

2) The use of CVD films

As mentioned in Chapter 3, although the exfoliated flakes may exhibit better quality, but due to the low yield process of mechanical exfoliation make it become less useful in the applications. Therefore, additional studies on heterostructures made of CVD graphene and CVD MoS_2 are undoubtedly important.

3) Development of better transfer techniques

Being the most challenging part of the entire project, a person's transfer skill will result in the good or bad quality of the final devices. A high quality heterostructures is the key for more advance researches and studies. In order to achieve higher mobility, from the technical point of view, further improvement and optimization of the current techniques are necessary.

References

[1] A.H. Castro Neto, et al. (2011) *New directions in science and technology: two-dimensional crystals*.

[2] A.H. Castro Neto, et al. (2011) *The electronics properties of graphene*.

[3] A.K. Geim (2013) *Van der Waals heterostructures*.

[4] Andrea C. Ferrari, et al. (2013) *Raman spectroscopy as a versatile tool for studying the properties of graphene*.

[5] Chen J.R. et al (2013) *Control of Schottky Barriers in Single Layer MoS$_2$ Transistors with Ferromagnetic Contacts*.

[6] Ernie W. Hill, et al. (2006) *Graphene Spin Valve Devices*.

[7] Huang X. et al. (2013) *Metal dichalcogenides nanosheets: preparation, properties and applications*.

[8] I. Wlasny, et al. (2012) *Optical contrast of single- and multi-layer graphene deposited on a gold substrate*.

[9] K.S. Novoselov (2012) *A roadmap for graphene*.

[10] K.S. Novoselov, et al. (2011) *Two-dimensional crystals-based heterostructures: materials with tailored properties*.

[11] Kallol Roy, et al. (2013) *Graphene-MoS$_2$ hybrid structures for multifunctional photoresponsive memory devices*.

[12] Kang J. (2012) *Graphene transfer: key for applications*.

[13] Larentis S. et al. (2014) *Band offset and negative compressibility in graphene-MoS$_2$ heterostructures*.

[14] Li H.M. et al. (2013) *Metal-Semiconductor Barrier Modulation for High Photoresponse in Transition Metal Dichalcogenide Field Effect Transistors*.

[15] P. Blake, et al. (2007) *Making graphene visible*.

[16] R.V. Gorbachev, et al. (n/a) *Hunting for Monolayer Boron Nitride: Optical and Raman Signatures*.

[17] Simone B. (2013) *Nonvolatile Memory Cells Based on MoS$_2$/Graphene Heterostructures*.

[18] Takehiro Y. et al. (2013) *Electrical Spin Injection into Graphene through Monolayer Hexagonal Boron Nitride*.

[19] William R.C. et al. (n/a) *Towards Fabrication of a Graphene MoS$_2$ junction*.

[20] Yuan H. et al. (2013) *Zeeman-type spin splitting controlled by an electric field*.

[21] Zhang Y.B. et al. (2005) *Experimental observation of the quantum Hall effect and Berry's phase in graphene*.

[22] Zhang Yi, et al. (n/a) *Direct observation of the transition from indirect to direct bandgap in atomically thin epitaxial MoSe$_2$*.